

## Recovery of siliceous ecosystems promoted Early Silurian climatic cooling

Huan Xu<sup>a</sup>, Bo Ran<sup>a,\*</sup>, Terry T. Isson<sup>b</sup>, Xinyang Chen<sup>a,c,d</sup>, Chao Luo<sup>e</sup>, Yi Li<sup>e</sup>, Yiqing Zhu<sup>e</sup>, Tong Sun<sup>a</sup>, Yuyue Han<sup>a,c,d</sup>

<sup>a</sup> State Key Laboratory of Oil and Gas Reservoir Geology and Exploitation, Chengdu University of Technology, Chengdu 610059, China

<sup>b</sup> Te Aka Mātūatua, University of Waikato (Tauranga), BOP, Tauranga, New Zealand

<sup>c</sup> Key Laboratory of Deep-time Geography and Environment Reconstruction and Applications of Ministry of Natural Resources and Institute of Sedimentary Geology, Chengdu University of Technology, Chengdu 610059, China

<sup>d</sup> International Center for Sedimentary Geochemistry and Biogeochemistry Research, Chengdu University of Technology, Chengdu 610059, China

<sup>e</sup> Shale Gas Research Institute of Petrochina Southwest Oil & Gas Field Company, Chengdu 610051, China



### ARTICLE INFO

Editor: H Falcon-Lang

**Keywords:**

Microcrystalline quartz  
Siliceous organisms  
Biogeochemical Si cycle  
Marine mudstone  
Early Silurian

### ABSTRACT

Throughout Earth's history, the delicate balance within the marine silicon cycle—between silicate weathering coupled to the formation of carbonate and chert versus reverse weathering—has been a fundamental driver of long-term climate stability. However, the ecological rise of siliceous organisms reduced the significance of this process in climate regulation during the Phanerozoic. Despite their importance, siliceous organisms are prone to diagenetic alteration, forming authigenic quartz, which makes direct study challenging. This study investigates Late Ordovician to Early Silurian marine mudstones, known for their richness in authigenic quartz, and uses high-precision scanning electron microscopy coupled with geochemical analyses. We find that the proportion of authigenic quartz (predominantly microcrystalline quartz) began to increase in the upper Hirnantian and reached a peak of 73.13 % in the Rhuddanian, exhibiting an inverse trend to previously reconstructed temperature variations. This microcrystalline quartz originates from the biogenic silica produced when siliceous organisms absorb dissolved silicon from seawater. Once deposited into sediment, it undergoes burial and dissolution, followed by nucleation and growth on micro-bleb (silicon-enriched extracellular polymers produced by microorganisms) surfaces or within locally supersaturated zones, eventually aggregating into ring-shaped clusters and aggregates. We speculate that the recovery of siliceous ecosystems in the Early Silurian provided sufficient silica for the formation of microcrystalline quartz, suppressing reverse weathering, which may have exacerbated or prolonged global cooling.

### 1. Introduction

The evolution of marine silicon cycling plays a critical role in regulating global climate stability and provides valuable insight to the evolution of life, in particular the advent of siliceous organisms (Kump et al., 2000; Bopp et al., 2005; Ikeda et al., 2017; Isson and Planavsky, 2018; Isson et al., 2020; Tréguer et al., 2021; Closset et al., 2022). The chief marine silicon removal pathways include authigenic clay formation (reverse weathering) and biogenic silica from biological processes, subsequently transformed from opal to microcrystalline quartz (Williams and Crerar, 1985; Williams et al., 1985; Conley et al., 2017; Isson and Planavsky, 2018; Isson et al., 2022; Ma et al., 2022).

Silicate weathering coupled to the formation of carbonate and chert acts to sequester carbon from the ocean-atmosphere system (Isson et al.,

2020). On the other hand, silicate weathering coupled to reverse weathering consumes alkalinity and acts to recycle carbon (Isson and Planavsky, 2018; Isson and Rauzi, 2024). On this basis, it is proposed that the balance of silicate weathering coupled to carbonate formation versus reverse weathering acts regulate the partial pressure of atmospheric CO<sub>2</sub> (Isson and Planavsky, 2018; Isson and Rauzi, 2024). It has been proposed that prior to the rise of siliceous life, a shift in this balance towards relatively more extensive reverse weathering may have played an important role in sustaining habitable largely ice-free conditions during the Precambrian (Isson and Planavsky, 2018; Isson and Rauzi, 2024). Since the Phanerozoic, the ecological rise of siliceous organisms (Kidder and Erwin, 2001; Conley et al., 2017; Deng et al., 2021) has strengthened the marine biological silicon pump, and in turn shifting the balance in favor of carbonate formation (Isson and Planavsky, 2018;

\* Corresponding author.

E-mail address: [ranbo08@cdut.cn](mailto:ranbo08@cdut.cn) (B. Ran).

Tréguer et al., 2017). However, the identification of siliceous organisms remains challenging, as many studies rely on drill core samples, where direct recognition is often difficult (Khan et al., 2019). Furthermore, post-depositional dissolution readily transforms siliceous remains into authigenic quartz (Williams and Crerar, 1985; Williams et al., 1985; Aller, 2014), introducing significant uncertainty in their identification and quantification. These limitations greatly hinder our ability to assess the climate-regulating role of siliceous organisms in the marine silicon cycle.

The Late Ordovician to Early Silurian represents a key interval of global climate change (e.g., Hirnantian glaciation; Finnegan et al., 2011) and biotic turnover (Krug and Patzkowsky, 2004; Chen et al., 2024), characterized by the extensive deposition of marine mudstones rich in authigenic quartz (Zou et al., 2019), making this a unique interval to investigate the influence of the marine silicon cycle on climate. By employing large-view field emission scanning electron microscopy (FE-SEM) splicing technology, quantitative evaluation of minerals by scanning electron microscopy (QEMSCAN), field-emission electron probe microanalysis (FE-EPMA), and geochemical analysis, this study investigates the origin and evolution of microcrystalline quartz, uncovering the implications of early marine silicon cycling for climate change.

## 2. Geological setting

The study area is located in the western part of the Yangtze Block in the South China Craton (Fig. 1). During the early-mid Paleozoic, the South China Craton was situated at the margin of the Gondwana near the paleo-equator (Metcalfe, 2006; Yao et al., 2015). Contemporaneously, the Yangtze Block was covered by a broad epeiric sea, while some areas were surrounded by the Qianzhong and Chuanzhong paleo-uplifts, forming a continental shelf sea (Chen et al., 2004; Yan et al., 2010). A succession of silica-rich marine mudstones, represented by the Wufeng–Longmaxi formations, was deposited from the Late Katian to Aeronian stages (Chen et al., 2004). Graptolite biostratigraphy provides standard criteria for the correlation of Ordovician–Silurian succession (Chen et al., 2004). This study utilized the graptolite biozone established from well W202, combined with gamma-ray (GR) log data, to reconstruct the upper Ordovician to Silurian successions for wells Y205 and Y206 (Fig. 2; Liang et al., 2025). In the Late Katian stage (most of Wufeng Formation), the Yangtze Block served as a major depocenter for the accumulation of the organic-rich Wufeng Formation (Yan et al.,

2015). The Hirnantian stage (from the uppermost Wufeng to the lowermost Longmaxi Formation) is characterized by generally thin sedimentary successions, typically less than 3 m in thickness, with widespread occurrences of limestones and Hirnantia brachiopod fauna (Chen et al., 2012). During the Rhuddanian–Aeronian interval (lower part of Longmaxi Formation), a global marine transgression occurred, resulting in the deposition of mudstones (Chen et al., 2018).

## 3. Samples and analytical methods

### 3.1. Samples

A total of 153 core samples were collected from three wells (Y205, Y206, and W202) in the South China Craton. The samples are predominantly composed of mudstone and are stratigraphically distributed from the Hirnantian to the Aeronian stages (Fig. 2).

### 3.2. Analytical methods

#### 3.2.1. QEMSCAN, large-view FE-SEM splicing technology and FE-EPMA

Thin sections were prepared for 153 samples and analyzed using Chengdu University of Technology's polarizing microscope under plane-polarized and cross-polarized light. Moreover, 19 core samples were cut into blocks measuring 8 × 8 × 3 mm and polished sequentially using sandpaper followed by an argon-ion polishing machine. Subsequently, the polished samples were coated with conductive carbon.

QEMSCAN and large-view FE-SEM splicing technology were performed using the Bruker XFlash 6130 and Gemini 450 instruments, respectively, at the Institute of Geology and Geophysics, Chinese Academy of Sciences. The surfaces of the argon-ion polished samples were scanned with an accuracy of 1 μm and a current greater than 1 nA to obtain backscattered electron images, secondary electron images, and mineral X-ray information. All mineral X-ray data were automatically matched with standard X-ray information to produce colour mineral images of different minerals. A region measuring 400 μm × 400 μm was selected on the BSE images according to the experimental purpose. A local fine scan was then performed using the field emission scanning electron microscope with a resolution of 4 nm, yielding high-resolution MAPS images that directly depict the size, shape, and distribution of minerals.

High-resolution backscattered electron images, energy-dispersive X-

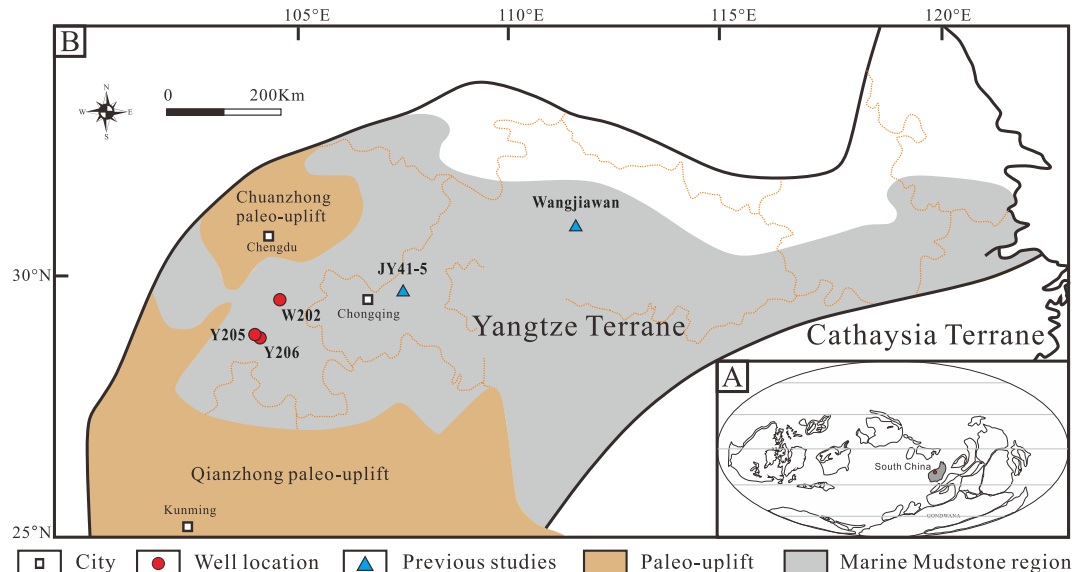


**Fig. 1.** (A) Paleogeographic map of the world across the Late Ordovician. (B) Paleogeographic map of the South China Craton. (Modified from Popov and Cocks, 2017; Han et al., 2021).

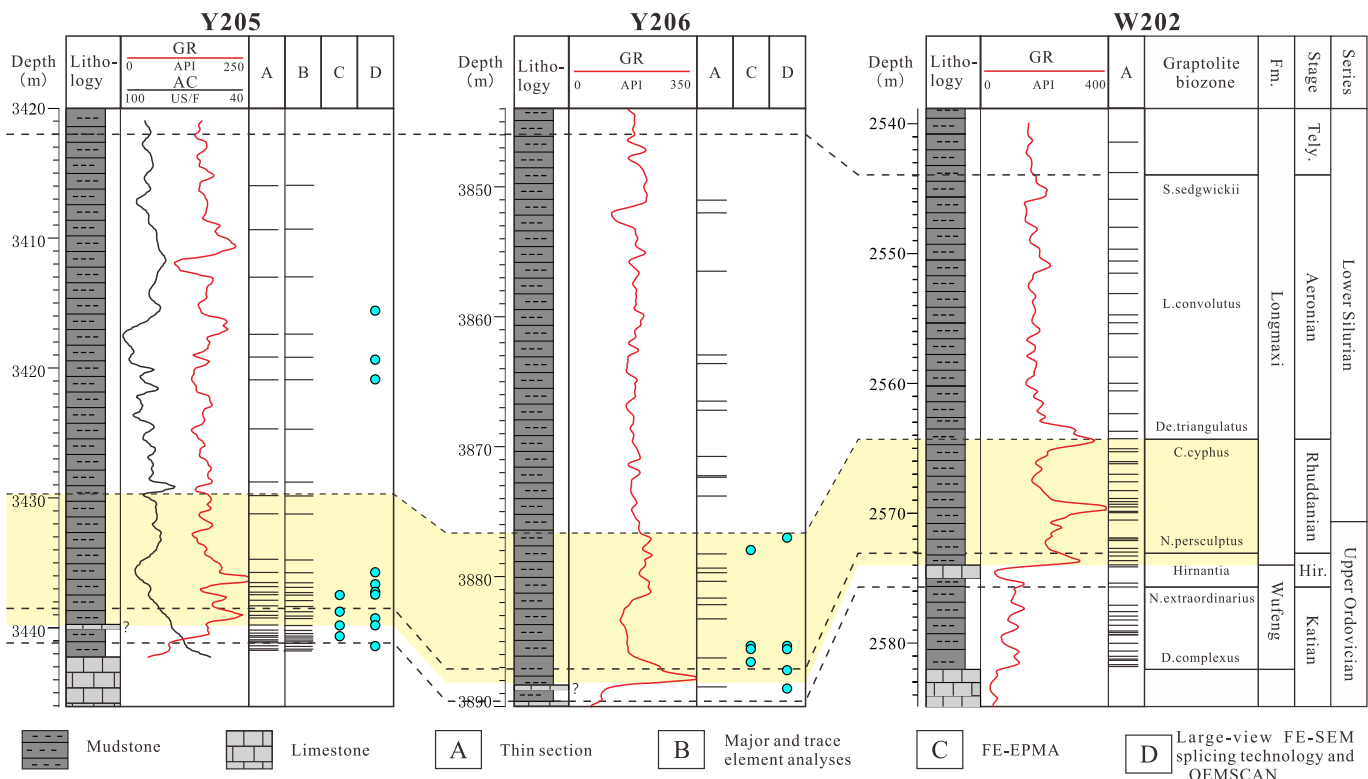


**Fig. 2.** Lithological columns of the three drill wells (Y205, Y206, and W202), along with the types and distribution locations of the sample analyses. Yellow represents the Upper Hirnantian-Rhuddanian; Fm. represents Formation. (For interpretation of the references to colour in this figure legend, the reader is referred to the web version of this article.)

ray spectroscopy analysis and elemental mapping were performed using an electron probe microanalyzer at SampleSolution Analytical Technology Co., Ltd., Wuhan, China. The instrument model used was Japan Electronics (JEOL) JXA-iHP200F. The analyses were conducted under the conditions of a beam current of  $2 \times 10^{-9}$  A, an accelerating voltage of 15 kV, and a beam diameter of 4  $\mu\text{m}$ .

### 3.2.2. X-ray diffraction, major and trace elements

X-ray diffraction (XRD) analysis was conducted on 77 bulk powder samples from Well Y205 using a Rigaku D/MAX 3C at Chengdu University of Technology. The instrument was operated at 40 kV and 30 mA. Diffraction data were collected over a  $2\theta$  range of  $5^\circ$  to  $70^\circ$ , with a step size of  $0.02^\circ$ . The  $2\theta$  precision of the instrument is better than  $\pm 0.01^\circ$ , and the detection limit for individual mineral phases is approximately 1–2 %.

Major and trace element analyses of 33 samples from well Y205 were conducted at ALS Chemex (Guangzhou) Co., Ltd. Major element analysis was performed by high-temperature fusion using a lithium borate–lithium nitrate flux, followed by determination with a PW2424 X-ray fluorescence (XRF) spectrometer. Calibration curves were established using certified reference materials GBW07105, NCSDC47009, and SARM-4. Both analytical precision and accuracy were better than 5 %. Trace element analyses were carried out using an Agilent 7900 inductively coupled plasma mass spectrometer (ICP-MS). Four internationally recognized reference materials—EMOG-17, GBM321-8, OREAS-45 h, and MRGeo08—were used to monitor analytical performance. Both precision and accuracy were within 10 % for most elements.

## 4. Results

### 4.1. Siliceous organisms

Siliceous organisms are typically present in marine fine-grained sedimentary rocks, including sponge spicules, radiolarians, and algae (Milliken and Day-Stirrat, 2013; Ergene, 2014). Under the microscope, sponge spicules (Fig. 3A and B) show distinct nearly perpendicular cross patterns, whereas algae (Fig. 3A and C) usually exhibit discrete spherical to elliptical shapes, and the radiolarians (Fig. 3D and E) exhibit typical spurs (Milliken et al., 2016, 2019). However, the characteristics of these siliceous organisms may not always be well-preserved and are often replaced by minerals such as quartz and calcite (Fig. 3C and E).

### 4.2. Whole rock composition and elemental composition

By employing whole-rock XRD and major and trace element data from Well Y205, we identified the quartz and clay content along with the variation of authigenic silica during the Late Ordovician to Early Silurian (Table S1; Fig. 4).

Quartz content during the Hirnantian to Aeronian stages exhibits a rise followed by a decline, peaking in the Rhuddanian, whereas clay content declines initially before rising, reaching its highest in the Aeronian (Fig. 4). In the Lower Hirnantian, the average quartz content is 22 %, and the average clay content is 11 %. In the Upper Hirnantian, the average quartz content is 51.1 %, and the average clay content is 8.2 %. In the Rhuddanian, the average quartz content is 49.2 %, and the average clay content is 20.4 %. In the Aeronian, the average quartz content is 33 %, and the average clay content is 27 %.

The analysis of major and trace elements reveals the concentrations of  $\text{SiO}_2$ ,  $\text{Si}_{\text{excess}}$ , Al, Ti, Mg, Ca and others (Table S1; Fig. 4).  $\text{SiO}_2$  ranges from 11.00 % to 77.21 %, with an average of 51.93 %. The excess silica variation is estimated using  $\text{Si}_{\text{excess}} = \text{Si}_{\text{sample}} - [(\text{Si}/\text{Al})_{\text{background}} \times \text{Al}]$

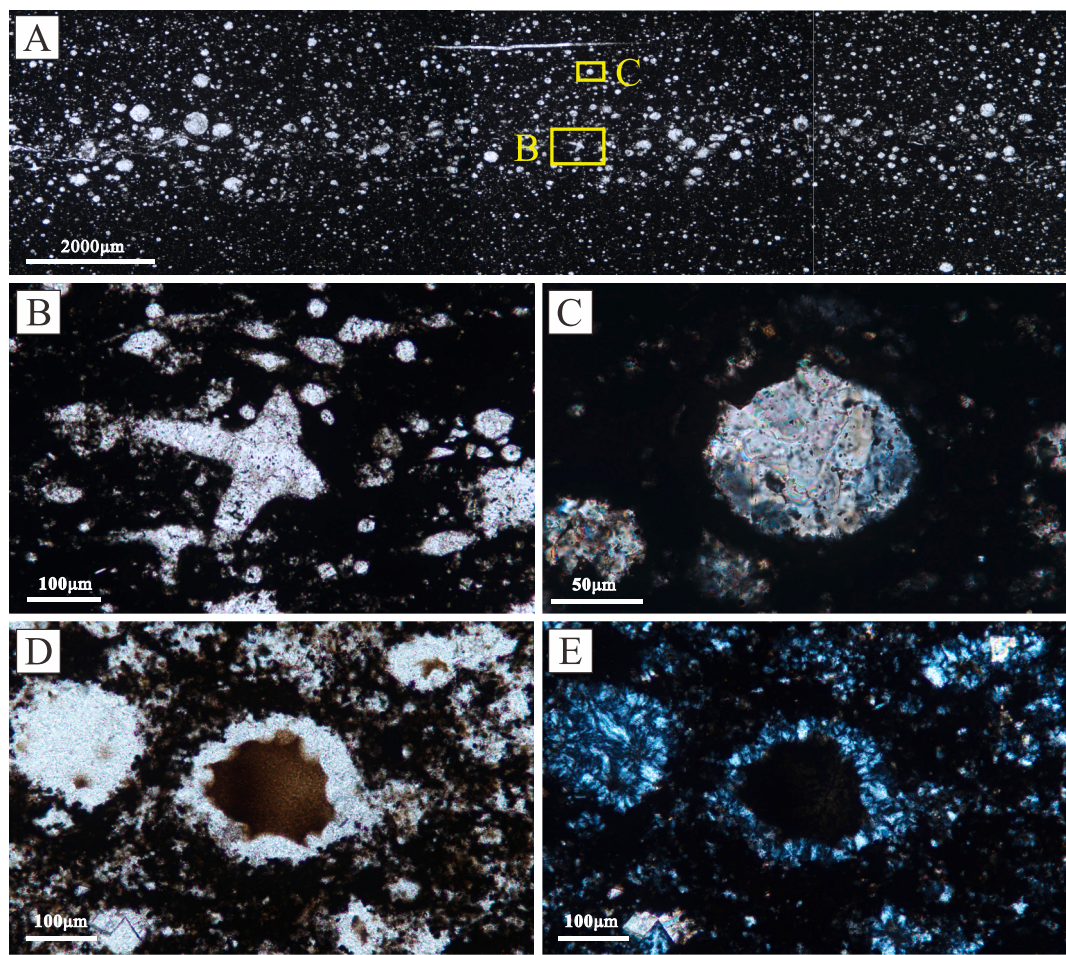


**Fig. 3.** Photomicrographs of Siliceous organisms. A = B = D: Plane-polarized light. C = E: Cross-polarized light. (A) Elliptical algae are densely distributed, containing a small amount of sponge spicules. (B) Displays nearly perpendicular intersecting sponge spicules. (C) Elliptical algae are extensively replaced by calcite. (D) and (E) Displays radiolarians with distinct spines, their shells replaced by silica. A = B = C: Y205, depth = 3438.76 m. D = E: W202, depth = 2579.86 m.

(sample)], with a background Si/Al ratio of 3.11 (Wedepohl, 1971). The Si<sub>excess</sub> values during the Hirnantian to Aeronian stages exhibit an increasing trend followed by a decrease, reaching a maximum in the Upper Hirnantian. In the Lower Hirnantian, the average Si<sub>excess</sub> is 7.72 %. In the Upper Hirnantian, it is 17.72 %. In the Rhuddanian, it averages 14.55 %, and in the Aeronian, it is 2.76 % (Fig. 4).

#### 4.3. Quartz types and contents

Petrographic analyses from multiple drill cores indicate that quartz in Late Ordovician–Early Silurian mudstones occurs in both detrital and authigenic forms, which can be distinguished using high-resolution electron microscopy (Fig. 5).

Detrital quartz is characterized by clay-silt grain sizes, sub-angular to sub-rounded shapes, and features such as secondary overgrowth (Milliken et al., 2016; Dowey and Taylor, 2017; Qiu et al., 2020; Peng et al., 2024). Using FE-SEM and QEMSCAN, we identified and quantified the proportions of detrital and authigenic quartz (Fig. S1). The results indicate that detrital quartz accounts for only a small fraction of the total quartz content (Table S2; Fig. 4). In contrast, more than 90 % of the quartz is authigenic (Table S2; Fig. 4). High-resolution electron microscopy further indicates that authigenic quartz primarily consists of microcrystalline quartz, exhibiting three distinct distribution patterns: single grain distribution (Fig. S2), clustered distribution (Fig. S3), and aggregated distribution (Figs. S4 and S5).

Microcrystalline quartz grains, individually distributed and either hexagonal (Figs. S2A to S2D) or bipyramidal (Figs. S2E and S2F) in

shape, are extensively dispersed in organic matter, usually with diameters ranging from 1 to 3  $\mu\text{m}$  (Fig. S2).

Clustered quartz displays rings and slightly ring forms (Fig. 6A, B, D, E, G, H, I). These clusters of quartz are observed to consist of microcrystalline quartz, either hexagonal (Fig. 6C) or bipyramidal (Fig. 6F), primarily existing in edge-to-face or face-to-face arrangements (Fig. 6). Additionally, some microcrystalline quartz is not just in simple contact but is interconnected (Fig. 6C and I).

The abundant authigenic quartz occurs as aggregates with straight boundaries, ranging from 100  $\mu\text{m} \times 200 \mu\text{m}$  in size (Fig. S4A). QEMSCAN analysis reveals that these aggregates are composed almost entirely of pure quartz, with only minor organic matter inclusions (Fig. S4B and S4C). Quartz aggregates possess the following characteristics: (1) The internal and external edge of the aggregates are straight (Fig. 7A and B). (2) The aggregate contains interconnected individual hexagonal microcrystalline quartz grains (1–3  $\mu\text{m}$  in diameter), with no significant other minerals at the connections or in the surrounding areas (Fig. 7C). (3) Within the aggregate, there are pores shaped as triangles, quadrilaterals, or even polygons (Fig. 7D). (3) There are extensively straight contours inside the aggregates (some of which are typical hexagonal), with pores developing inside these contours (Fig. 7E and F).

## 5. Discussion

### 5.1. Dynamic mechanism of microcrystalline quartz cementation

Previous reports, due to the small size of marine mudstone grains,

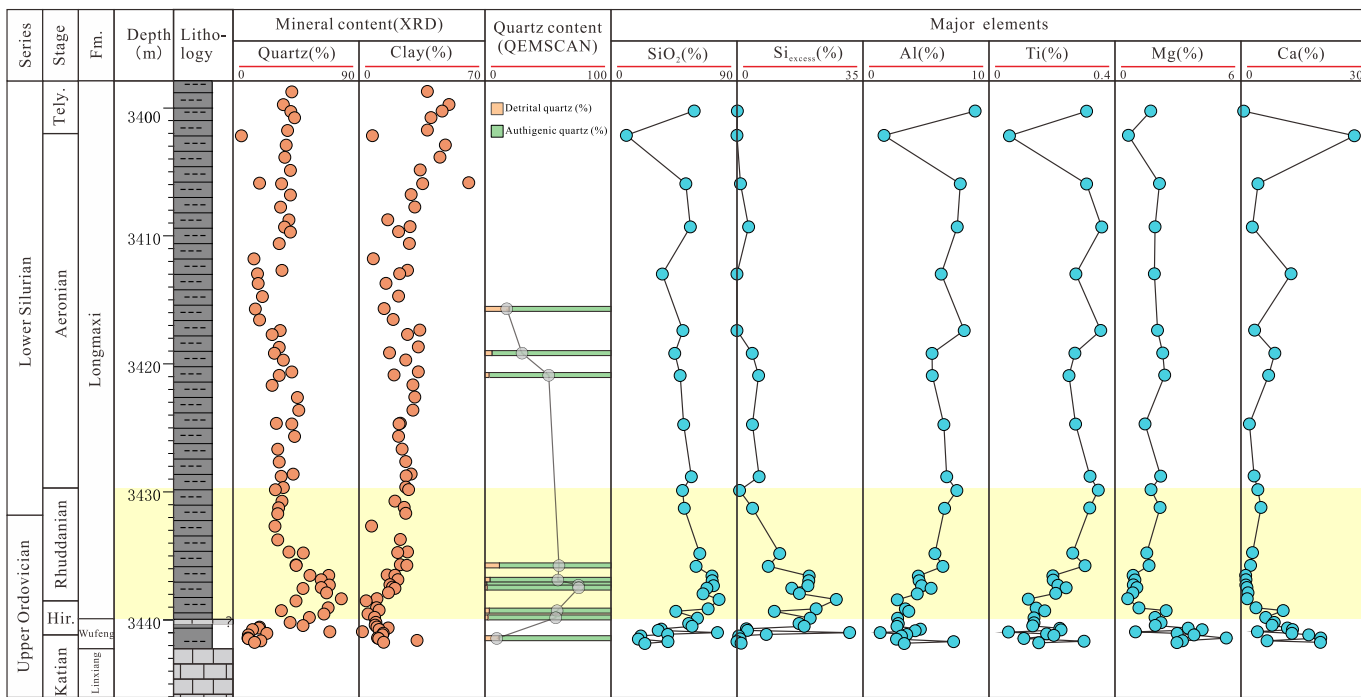


**Fig. 4.** Quartz and clay, authigenic and detrital quartz, and major elements ( $\text{SiO}_2$ ,  $\text{Si}_{\text{excess}}$ ,  $\text{Al}$ ,  $\text{Ti}$ ,  $\text{Mg}$ ,  $\text{Ca}$ ) the Katian-Aeronian in Well Y205. Yellow represents the Upper Hirnantian-Rhuddanian; Fm. represents Formation. (For interpretation of the references to colour in this figure legend, the reader is referred to the web version of this article.)

mainly focused on the formation of single-grain microcrystalline quartz (Williams et al., 1985; Worden et al., 2012) or the formation of pore support through the contact of numerous microcrystalline quartz grains (Milliken and Day-Stirrat, 2013; Milliken and Olson, 2017; Emmings et al., 2020; Peng et al., 2024). However, few papers have documented the dynamic evolution process of why or how microcrystalline quartz cements in marine mudstone.

Isolated microcrystalline quartz can be found in marine mudstone (Milliken and Olson, 2017), but more commonly, microcrystalline quartz is intergrown in clusters or aggregates (Figs. 6 and 7; Figs. S4 and S5). Microcrystalline quartz and clustered quartz are transitional in some degree (Folk, 1974). Experimental studies have shown that the decline in the surface precipitation rate when quartz monocrystalline grains grow to achieve a fully euhedral form (Lander et al., 2008). It is unlikely that the euhedral microcrystalline quartz would stop growing, but rather form overgrowth through cementation on its surface (Figs. 6 and 7). As documented by Qiu et al. (2020) through SEM and SEM-CL images, the microcrystalline quartz in marine mudstone of the Late Ordovician to Early Silurian features a bluish euhedral core surrounded by an orange syntaxial overgrowth, suggesting that the bluish small-grained microcrystalline quartz in the core experienced overgrowth. Moreover, the apparent interlocking of adjacent microcrystalline quartz grains within the aggregate in the study area suggests that the microcrystalline quartz has undergone cementation (Figs. 7A to 7C; Folk, 1974; Thyberg et al., 2010; Dowey and Taylor, 2017; Milliken and Olson, 2017).

Quartz cementation is strongly influenced by temperature, with quartz being the main cement in rocks buried at temperatures over 70–80 °C (depths of 2000–2500 m), a fact confirmed in both sandstones (Bjørlykke and Egeberg, 1993; Worden and Morad, 2000) and mudstones (Peltonen et al., 2009; Thyberg et al., 2010). Marine mudstones from the Late Ordovician to Early Silurian in the study area exhibit high thermal maturity and deep burial characteristics, with peak burial temperatures reaching 190–200 °C (Liu et al., 2021). Consequently, influenced by factors such as temperature, compaction, and pore space, intergranular cementation by microcrystalline quartz is possible. The

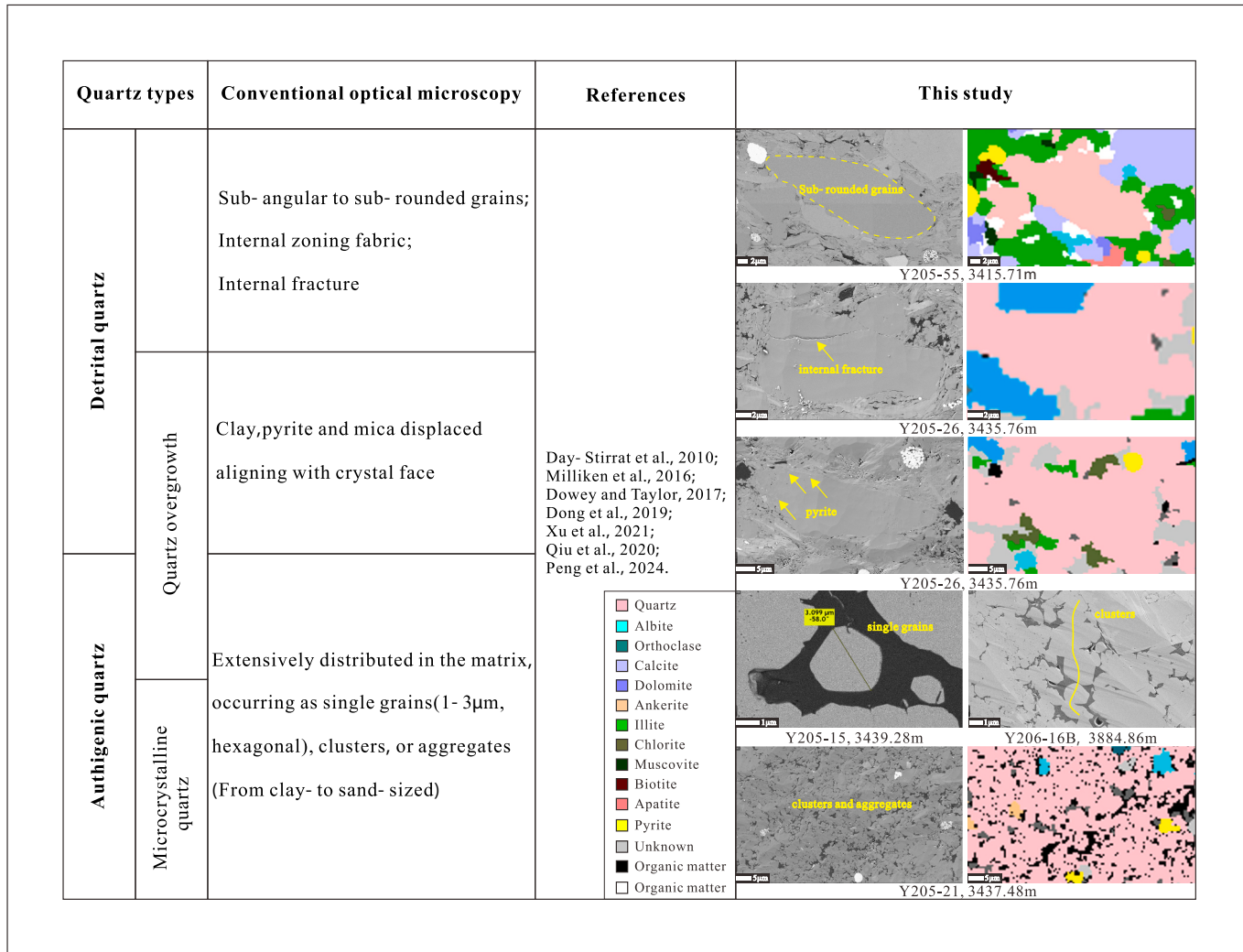
occurrence of euhedral microcrystalline quartz grains within authigenic quartz clusters and aggregates thus suggests that the microcrystalline quartz may have grown from single grains into aggregates during diagenesis (Figs. S2 to S5).

Fig. 8 illustrates the potential sequence of diagenetic events starting with the initial precipitation of euhedral microcrystalline quartz (Fig. 8A). The next step is to form a touch framework (clusters) due to the accumulation of microcrystalline quartz, which may also be affected by compaction (Fig. 8B; Burland, 1990; Velde, 1996). Quartz cement forming as syntaxial quartz overgrowth is the key to the interconnection of microcrystalline quartz (Fig. 8C; Qiu et al., 2020). Due to the mutual cementation of euhedral microcrystalline quartz, small pores are left within the straight contours (Fig. 8C and D). The cementation of microcrystalline quartz will continue to grow until filling the available pore space, provided there are adequate conditions of silica and time (Fig. 8D).

## 5.2. The main silica source of microcrystalline quartz and its cement

Previous studies have reported that the common sources of microcrystalline quartz in mudstones include the dissolution of biogenic silica (Schieber et al., 2000; Milliken et al., 2012; Milliken and Olson, 2017), the illitization of smectite (Peltonen et al., 2009; Thyberg et al., 2010; Metwally and Chesnokov, 2012; Dowey and Taylor, 2017, 2020), and hydrothermal input (Adachi et al., 1986). However, most microcrystalline quartz in Late Ordovician–Early Silurian mudstones is interpreted as biogenic, based on the morphology of quartz and whole-rock geochemical evidence.

Clusters (Fig. 6) or larger aggregates (Fig. 7; Fig. S4 and S5) composed of microcrystalline quartz are widely distributed in the Upper Hirnantian to Rhuddanian stages. The clusters of microcrystalline quartz display ring or slightly ring forms (Fig. 6), indicating that nucleation occurred on dissolved, unidentified skeletal fragments (Milliken and Olson, 2017). The evidence is corroborated by the widespread occurrence of siliceous bioclastic debris, including radiolarians and sponge spicules (Fig. 3). The dissolution of siliceous organisms creates high



**Fig. 5.** Petrographic characteristics of quartz types that are commonly observed in organic-rich mudstones (Day-Stirrat et al., 2010; Milliken et al., 2016; Dowey and Taylor, 2017; Dong et al., 2019; Xu et al., 2021; Qiu et al., 2020; Peng et al., 2024).

silicon saturation, which promotes the continuous nucleation and growth of microcrystalline quartz within mudstones (Williams et al., 1985; Bjorkum and Nadeau, 1998; Bjørlykke, 1998). Crystals of microcrystalline quartz nucleate on appropriate substrates, including early-formed microcrystalline quartz, resulting in larger aggregates of microcrystalline quartz. Additionally, microcrystalline quartz aggregates nearly entirely exclude other mineral phases, like mica and clays (Fig. 7; Figs. S4 and S5), which mechanical sorting processes struggle to account for. Although diagenesis of clay minerals could potentially supply silica, the low permeability and significant overburden pressure of the mudstones (Jin et al., 2014) render the contribution of silica from external or internal clay, feldspar, or other minerals almost impossible. This interpretation is further supported by the low clay content recorded during the Upper Hirnantian to Rhuddanian stages. Therefore, the most likely interpretation is that the microcrystalline quartz and the clusters or aggregates derived from it are of biogenic source.

Whole-rock major and trace element geochemistry is widely used to distinguish between hydrothermal and non-hydrothermal silica, as well as between biogenic and terrigenous sources (Adachi et al., 1986; Wright et al., 2010; Gambacorta et al., 2016; Dong et al., 2019). Firstly, the relative abundances of Al-Fe-Mn on a ternary diagram provide an effective means of discriminating hydrothermal from non-hydrothermal silica (Adachi et al., 1986). In this study, consistent with previous research, mudstone samples from the Upper Hirnantian to Rhuddanian

stages primarily plot within the non-hydrothermal field (Fig. 9A; Yan et al., 2009; Liang et al., 2025), indicating that the silica during this interval is not of hydrothermal sources. Secondly, the relationship between SiO<sub>2</sub> and Zr has been widely used to distinguish biogenic from terrigenous silica sources (Wright et al., 2010; Gambacorta et al., 2016; Dong et al., 2019). A significant negative correlation between SiO<sub>2</sub> and Zr is generally interpreted as an indicator of biogenic sources, as demonstrated in the Muskwa Formation, which is known for its high biogenic silica input (Wright et al., 2010). This study, a strong negative correlation is observed during the Upper Hirnantian to Rhuddanian stages ( $R^2 = 0.6680$  and  $0.9235$ , respectively), suggesting that silica in these intervals was mainly derived from biogenic sources (Fig. 9B). In contrast, positive correlations observed during the Lower Hirnantian and Aeronian stages imply a greater contribution from terrigenous sources (Fig. 9B). Furthermore, stable silicon isotopes provide an additional line of evidence for identifying silica sources (Van den Boorn et al., 2007). Previous studies have presented systematic analyses of  $\delta^{30}\text{Si}$  values from mudstones of the Upper Hirnantian to Rhuddanian stages in South China (Han, 2018; Zan et al., 2024). For comparison,  $\delta^{30}\text{Si}$  data were also compiled from Katian cherts, Aeronian-Telychian bedded cherts, radiolarians, and sponge spicules (Trower et al., 2021). The  $\delta^{30}\text{Si}$  values of the studied mudstones ( $-0.2\text{ ‰}$  to  $0.17\text{ ‰}$ ) fall within the range of biogenic chert from the Aeronian to Telychian stages ( $-0.8\text{ ‰}$  to  $1.6\text{ ‰}$ ; Fig. 9C). These results further support the

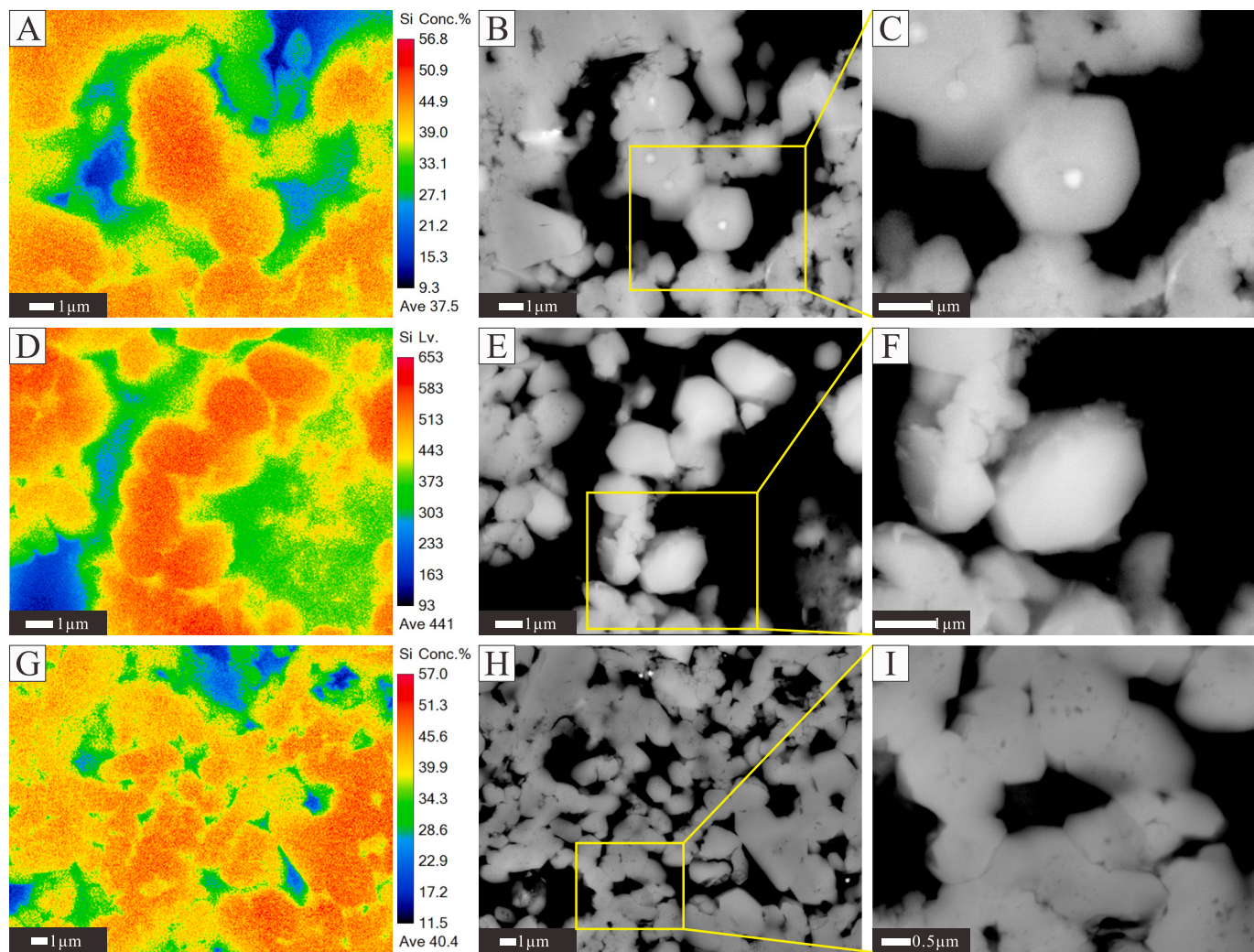


**Fig. 6.** FE-EPMA (BSE + EDS + elemental mapping) images of typical euhedral microcrystalline quartz grains on authigenic quartz clusters. Clusters of micro-crystalline quartz display rings and slightly ring forms. A = B = C: Y206, depth = 3886.58 m. D = E = F: Y206, depth = 3886.58 m. G = H = I: Y205, depth = 3438.76 m.

interpretation that the silica during the Upper Hirnantian to Rhuddanian interval was primarily derived from biogenic sources. Therefore, petrographic and geochemical evidence indicates that siliceous organisms constitute the main source of microcrystalline quartz and its cement in the mudstones from the Upper Hirnantian to Rhuddanian.

### 5.3. Reconstruction of the marine silicon cycle in the Early Silurian

Silicon originally derived from crustal weathering enters the ocean through six key pathways, including rivers, submarine groundwater, minerals, aeolian deposition, glacial meltwater, and hydrothermal inputs, predominantly in the form of dissolved silicon (Trégouer and De La Rocha, 2013; Trégouer et al., 2021). Previous studies have demonstrated that the primary sinks for dissolved silicon in the ocean are reverse weathering—leading to the formation of authigenic clays—and the biological silicon pump, which drives the burial of biogenic silica (Isson and Planavsky, 2018; Isson et al., 2020; Isson et al., 2022; Trégouer et al., 2017). However, previous research has predominantly centered on the formation of authigenic quartz (Milliken et al., 2016; Milliken and Olson, 2017; Emmings et al., 2020; Qiu et al., 2020; Peng et al., 2024; Nie et al., 2025), with limited attention paid to the substantial role that authigenic clay formation may play in the sequestration of dissolved silicon. This significant oversight has posed a major constraint on accurately reconstructing the marine silicon cycle.

The clay mineral assemblages of marine mudstones from different geological periods indicate that illite was the dominant clay mineral during the Late Ordovician to Early Silurian (Weaver, 1967; Chen et al., 2023; Huang et al., 2023). FE-SEM observations reveal that the illite in the samples exhibit a platy morphology with preferred orientation and pronounced cleavage, with some flakes displaying curvature attributed to compaction—features characteristic of a typical terrigenous input (Fig. 10A and B, Meunier and Velde, 2013; Rafiei et al., 2020). Previous studies have shown that detrital clays typically have much lower Li/Th and Al/Th ratios compared to authigenic clays (Yin et al., 2023). Therefore, the geochemical composition of the study area samples was compared with both modern and ancient detrital sedimentary rocks to investigate the provenance of the clays. The results indicate that the clay minerals in the study area are more consistent with a detrital origin (Fig. 10C). In addition, Sc and Ti show strong correlations with Al in the samples, and the Al/Sc and Al/Ti ratios are close to the average values of the upper continental crust (Fig. S6). This is consistent with known detrital clays in the Datangpo Formation (Wei et al., 2020), suggesting that the contribution of marine authigenic clays is negligible. Therefore, both petrographic and geochemical evidence suggest that during the Early Silurian, dissolved silicon in the ocean was more likely buried in the form of biogenic silica derived from siliceous organisms rather than as authigenic clay (Fig. 11).

Radiolarians have long been regarded as important indicators of

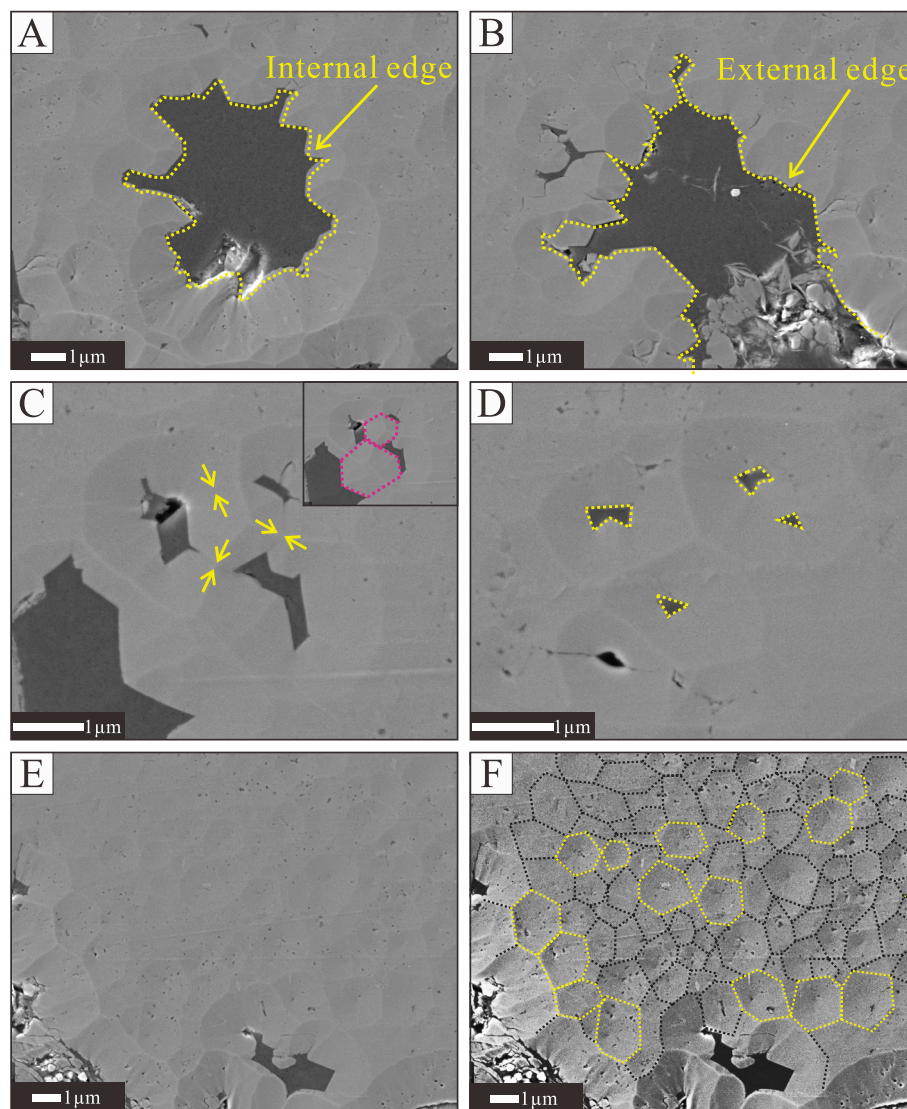


**Fig. 7.** Large-view FE-SEM splicing technology showing the microscopic characteristics of authigenic quartz aggregates. Y205, depth = 3439.28 m. (A) Illustrates the straight internal edge of the quartz aggregate (yellow dashed line). (B) The external edge of the quartz aggregate is also straight, and visible single grain quartz partially (yellow dashed line). (C) Typical hexagonal microcrystalline quartz grain occurs in interconnection within the aggregates (purple dashed lines), and the contact of grains is straight and clean (yellow arrows). (D) Triangle and polygonal pores occur at the flat edge of the aggregate (yellow dashed lines). (E) and (F) Extensive straight contour appear in quartz aggregates (black dashed lines), some of which exhibit typical hexagonal shapes (yellow dashed lines). (For interpretation of the references to colour in this figure legend, the reader is referred to the web version of this article.)

upwelling activity in both ancient and modern studies (Pichevin et al., 2014; Ran et al., 2015; Zhang et al., 2018). Both this study and previous research suggest that the study area experienced vigorous upwelling, which connected to the open ocean and enhanced the productivity of siliceous organisms (Fig. 11; Ran et al., 2015; Zhang et al., 2018). Siliceous organisms such as radiolarians contributed to the export of dissolved silicon, which subsequently underwent dissolution and oversaturation-driven precipitation near or slightly below the sediment–water interface, leading to the formation of microcrystalline quartz. However, Delle Piane et al. (2022) reported the presence of vesicle-like nuclei in microcrystalline quartz within Early Silurian black shales, which challenges the conventional view that microcrystalline quartz forms solely through the dissolution–reprecipitation of siliceous biogenic material. Notably, these vesicles resemble the silicon-rich extracellular polymeric substances (EPS) secreted by microorganisms, as confirmed by Tang et al. (2014). This resemblance suggests that microbial processes may have played a significant role in the burial of dissolved silicon. Studies have shown that microorganisms such as

cyanobacteria can secrete extracellular polymeric substances that are enriched in silicon and capable of forming micro-blebs (Kazmierczak et al., 2012; Tang et al., 2014). It is worth noting that these micro-blebs may act not only as sources of silicon (Jurkowska and Świerczewska-Giadysz, 2020; Jurkowska and Świerczewska-Giadysz, 2024) but also as favorable interfaces and nucleation sites for silicon precipitation (Williams and Crerar, 1985; Benning et al., 2004; Handley et al., 2008). Therefore, in sediments, silicon derived from the dissolution of siliceous organisms such as radiolarians may nucleate on the surfaces of micro-blebs or within pore waters locally supersaturated with respect to silica, leading to the formation of microcrystalline quartz, which ultimately aggregates into larger assemblages (Fig. 11).

#### 5.4. Regulatory role of siliceous organisms in Early Silurian climate dynamics

The sustained anomalous high temperatures following the Late Permian-Early Triassic mass extinction have been explained by the

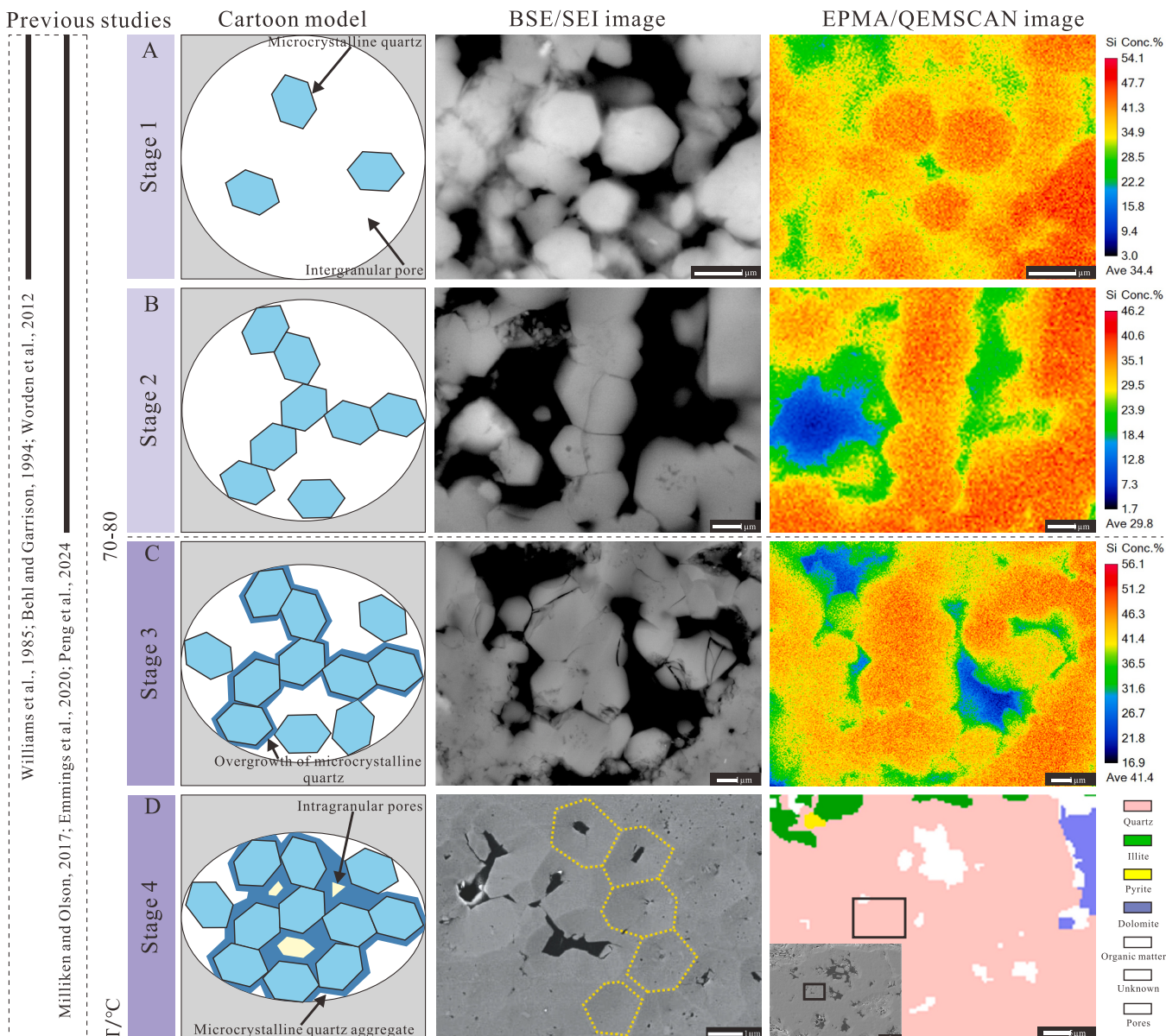


**Fig. 8.** Model showing (from A to D) the dynamic evolution process of quartz cementation on microcrystalline quartz surfaces. (A) During early diagenesis, equant microcrystalline quartz (1–3  $\mu\text{m}$ ) forms and widely fills primary pore spaces. Y206, depth = 3886.58 m. (B) Microcrystalline quartz grains accumulate into a rigid touching framework with ring or partial ring forms, supporting micron-scale pore spaces. Y205, depth = 3438.76 m. (C) Microcrystalline quartz is cemented to form an interconnected framework, which is stronger than ring or partial ring framework. These have the same crystallographic orientation as the microcrystalline quartz grains and are used to fill and close polygonal pore spaces. Y205, depth = 3438.76 m. (D) During late diagenesis, microcrystalline quartz continues to cement and fill pore spaces, and some triangular and quadrilateral pores may be residual. Y205, depth = 3439.28 m.

collapse of marine siliceous ecosystems, which weakened the suppression of reverse weathering (Isson et al., 2022). This is further supported by the reduction in quartz (mainly biogenic silica) content and an increase in cation-rich clay minerals (Isson et al., 2022). In contrast, after the Late Ordovician-Early Silurian mass extinction event driven by the Hirnantian glaciation (Sheehan, 2001; Finnegan et al., 2011), authigenic quartz (predominantly microcrystalline quartz) in the Rhuddanian increased and reached its peak, while clay content remained low, coinciding with sustained cold climatic conditions (Fig. 12; Frakes et al., 1996; Trotter et al., 2016; Rasmussen et al., 2019). Several hypotheses have been proposed to explain the climate change, including silicate weathering (Longman et al., 2021), organic carbon burial (Longman et al., 2021; Zhang et al., 2024; Lv et al., 2025), volcanic activity (Lv et al., 2022; Yang et al., 2022), and orbital forcing (Herrmann et al., 2003). However, the Hirnantian glaciation is generally believed to have

been primarily driven by an increase in organic carbon burial (Brenchley et al., 1994; Longman et al., 2021; Zhang et al., 2024). Multiple global stratigraphic records reveal a significant negative shift in inorganic carbon isotopes from the upper Hirnantian to the Rhuddanian (Fig. S7). This may have been attributed to organic carbon degradation related to microbial sulfate reduction and/or methanogenesis/anaerobic oxidation of methane, as demonstrated by Chen et al. (2017) and Chen et al. (2020). Therefore, it is unlikely that the cold climate during the Rhuddanian was primarily driven by enhanced organic carbon burial. Here, we propose a potentially new mechanism—recovery of siliceous organisms that suppressed clay formation through reverse weathering (Fig. 12). This mechanism is plausible because a reduction in reverse weathering, which consumes alkalinity, cations, and reactive silica while forming clays and releasing  $\text{CO}_2$ , could lead to a decrease in atmospheric-oceanic  $\text{CO}_2$  partial pressure (Isson and Planavsky, 2018).

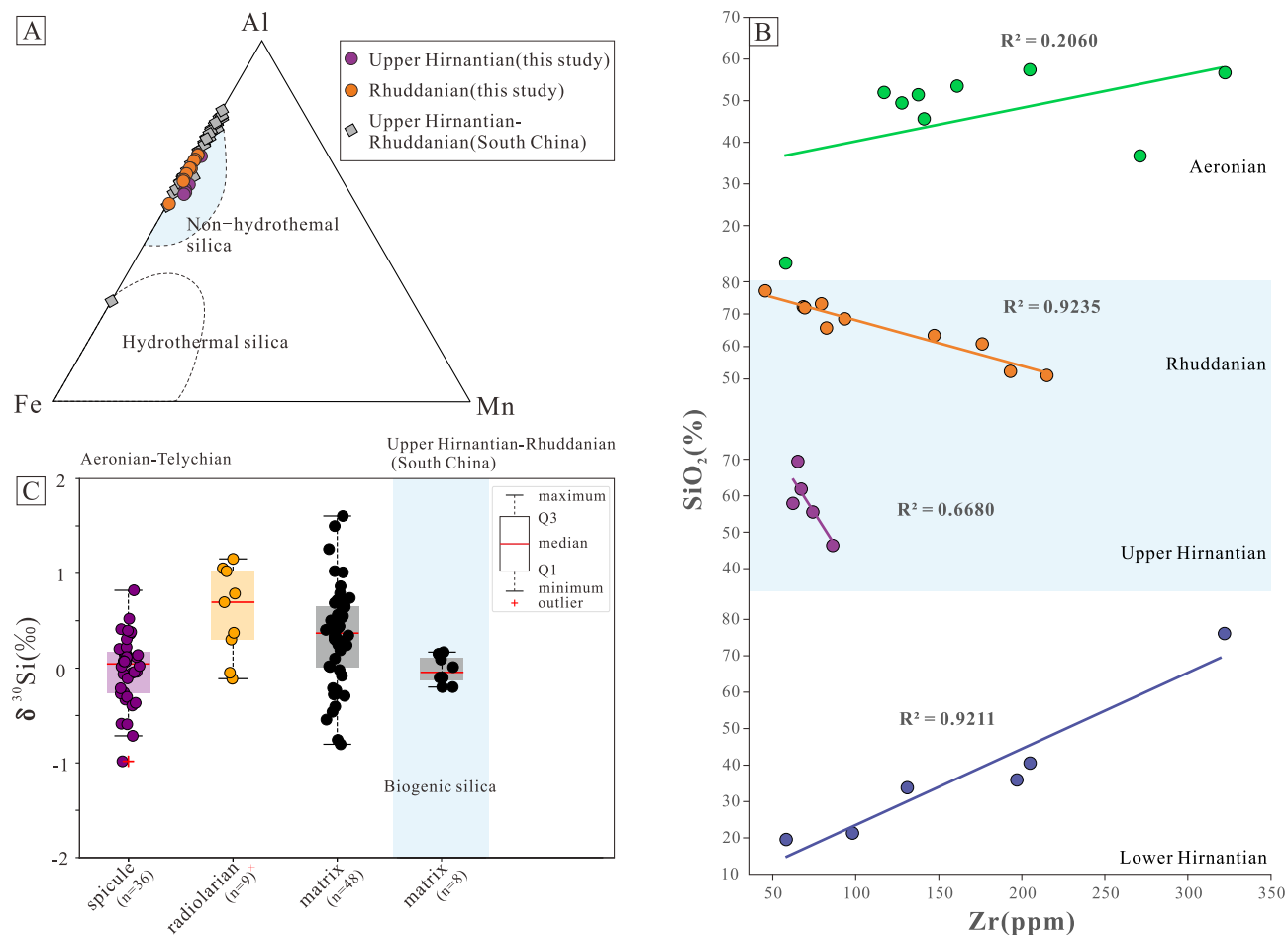


**Fig. 9.** Elemental and isotopic features of Early Silurian mudstones in South China in this study and previous studies. (A) All mudstone samples from the Upper Hirnantian to Rhuddanian stages in this study plot within the “non-hydrothermal silica” field on the Al–Fe–Mn ternary diagram (Yan et al., 2009; Liang et al., 2025). (B) A significant negative correlation between Zr and SiO<sub>2</sub> is observed in the same samples, indicating a primarily biogenic origin of the silica. (C) A box plot of δ<sup>30</sup>Si values for mudstones from the Upper Hirnantian to Rhuddanian stages in South China is presented (Han, 2018; Zan et al., 2024), along with δ<sup>30</sup>Si data for radiolarians, sponge spicules, and chert matrix from the Aeronian–Telychian intervals (Trower et al., 2021).

Authigenic quartz content increased from the upper Hirnantian and peaked in the Rhuddanian, predominantly occurring as microcrystalline quartz in clustered or aggregate forms (Fig. 12). This trend closely aligns with previously quantified variations in siliceous organisms and excess silica (Khan et al., 2019; Deng et al., 2021), suggesting that authigenic quartz content could serve as a reliable proxy for siliceous organism abundance, overcoming limitations in biostratigraphic identification and quantification from drill cores. Additionally, global stratigraphic and drilling records indicate a consistent trend in excess silica variations (Fig. S8), suggesting that the recovery of siliceous organisms was likely a global event.

The recovery of siliceous organisms has driven dissolved silicon to preferentially convert into biogenic silica, effectively decoupling the available dissolved silicon from the cations necessary for clay formation (Dunlea et al., 2017; Isson and Planavsky, 2018). Although the dissolution of biogenic silica within sediments may also act as a source of silicon for authigenic clay minerals, porewater data from modern continental shelf, slope, and deep-sea sites indicate that, even in areas with high biogenic silica content, dissolved Si(OH)<sub>4</sub> concentrations are generally too low to sustain extensive marine authigenic clay mineral formation (Isson and Planavsky, 2018). Such a decoupling is therefore likely to impose both spatial and kinetic constraints on the reverse weathering processes. This interpretation is further supported by the low abundances of clay minerals—dominated by terrestrial detritus—observed in the study area. Furthermore, Dunlea et al. (2017)

demonstrated that a weakening of reverse weathering in the Cenozoic led to reduced seawater Mg removal, resulting in an increase in seawater Mg/Ca ratios. Given the differences between the Cenozoic and Paleozoic, we investigated known intervals of strengthened or weakened reverse weathering in the Cenozoic and Mesozoic, specifically at Site U1370 and the Akkamori section, and found similar Mg/Ca trends (Fig. S9). Therefore, the observed increase in Mg/Ca ratios across multiple Paleozoic stratigraphic sections and drill cores may also indicate a weakening of reverse weathering, although variations in reverse weathering intensity may result in substantial fluctuations in the Mg/Ca range. Notably, the recovery of siliceous organisms may have suppressed reverse weathering, thereby lowering the atmosphere–ocean pCO<sub>2</sub>, a trend that aligns well with previously reconstructed sea surface temperatures and global mean surface temperatures during the upper Hirnantian to Rhuddanian stages (Fig. 12; Trotter et al., 2016; Rasmussen et al., 2019; Judd et al., 2024). Although sea surface temperatures may have exhibited a transient increase due to volcanic activity (Yang et al., 2022), the overall trend remained one of decline, with temperatures falling below even the minimum values recorded during the Hirnantian glaciation (Fig. 12). Thus, the observed high authigenic quartz and low clay content from the upper Hirnantian to Rhuddanian, along with its consistency with previously reconstructed temperature trends, supports the hypothesis that the recovery of siliceous organisms inhibited reverse weathering, potentially exacerbating or prolonging global cooling.

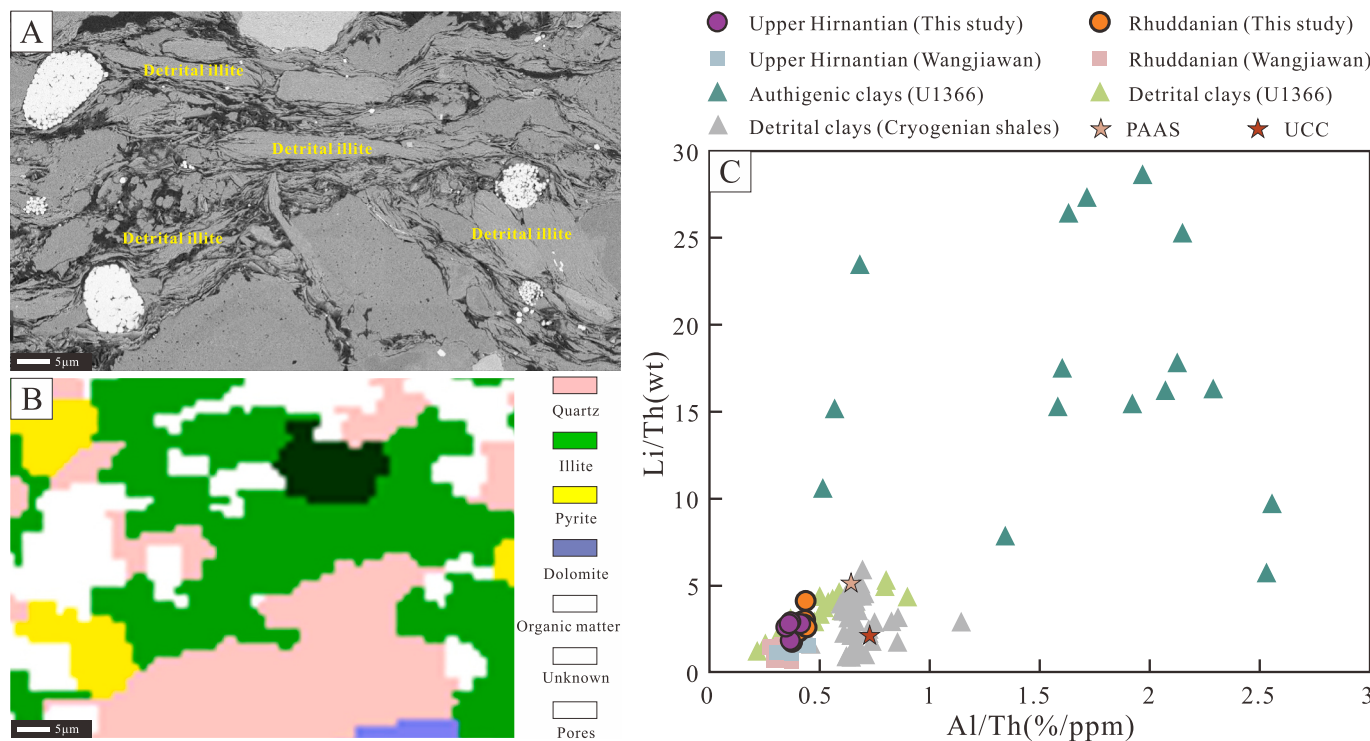


**Fig. 10.** Petrographic and geochemical analyses illustrate the identification of detrital and authigenic clays. (A) Large-view FE-SEM splicing technology reveals platy illite with distinct cleavage, some of which is bent due to compaction. Y205, depth = 3439.28 m. (B) Corresponding QEMSCAN results for image (A). (C) Cross-plot of Li/Th versus Al/Th for marine mudstones from the Upper Hirnantian to Rhuddanian stages in Well Y205, compared with other modern and ancient detrital sedimentary rocks, including IODP Site U1366 core samples (Dunlea et al., 2015), the Nantuo Formation shale from the Cryogenian Datango Formation (Wei et al., 2020), upper continental crust (UCC) (Rudnick and Gao, 2014), Post-Archean Average Shale (PAAS) (Taylor and McLennan, 1985), and mudstones from the Wangjiawan section (Yan et al., 2009).

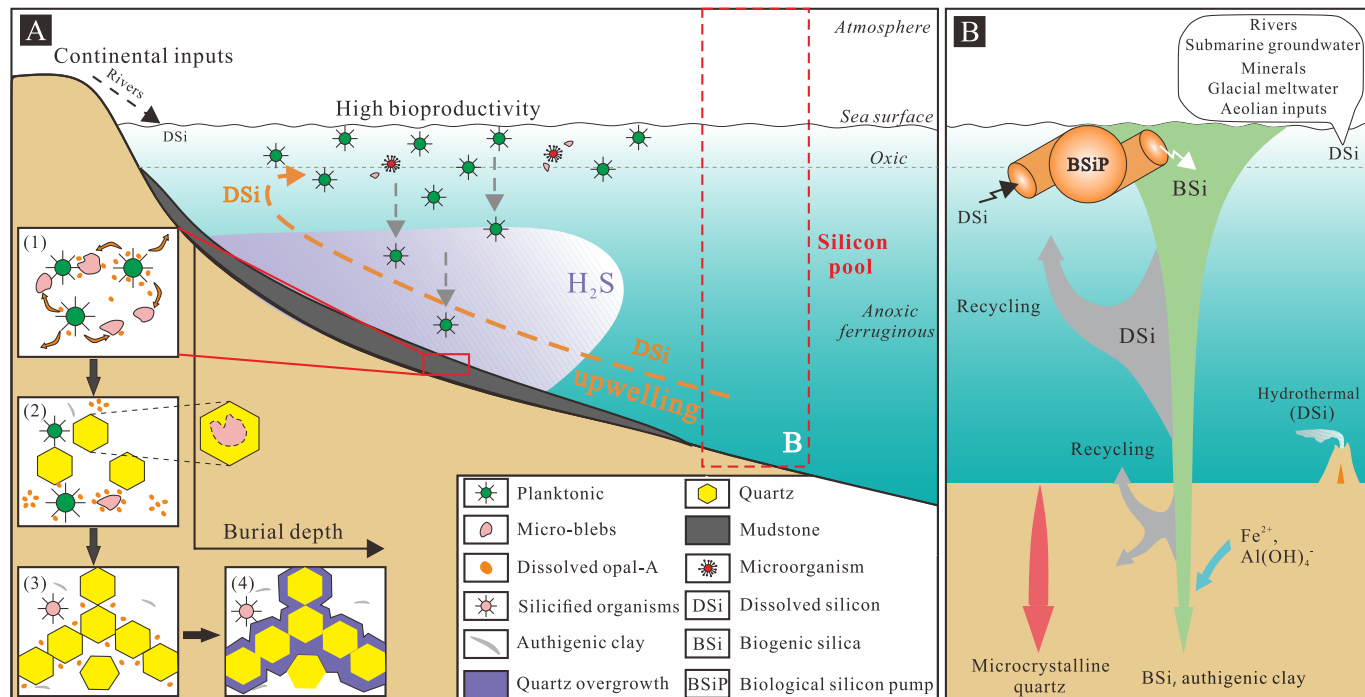


**Fig. 11.** A schematic representation of the marine silicon cycle in the Early Silurian (Upper Hirnantian to Rhuddanian). The figure shows the source of oceanic silicon, its existence, transformation, burial methods in the ocean, and the diagenetic evolution after burial.

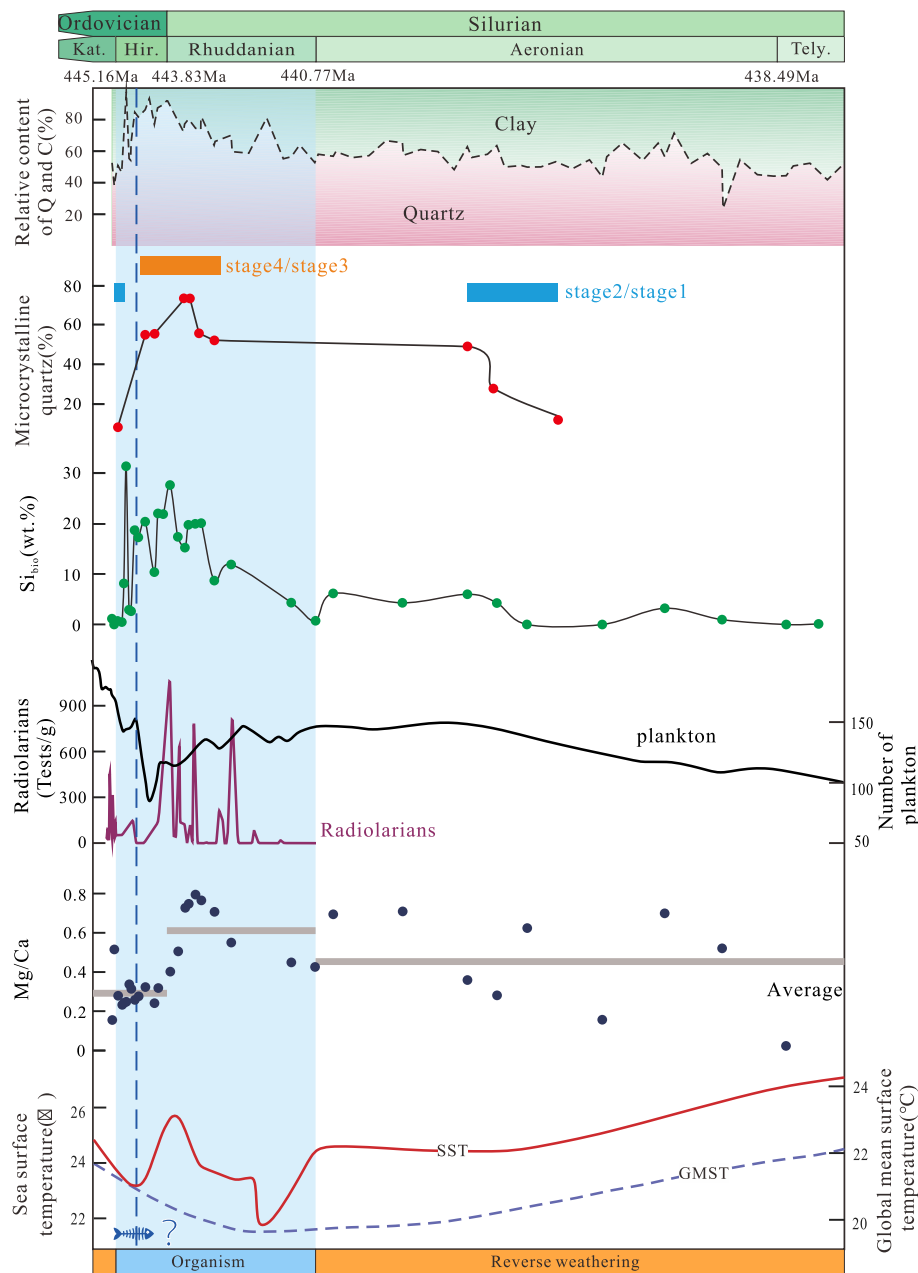


**Fig. 12.** The relative proportion of quartz (Q) to clay (C), microcrystalline quartz content, biogenic silica content, and Mg/Ca ratios in Well Y205 from the Late Ordovician to Early Silurian. The planktonic abundance in the South China Craton (Deng et al., 2021) and the radiolarian abundance in Well JY41–5 (Khan et al., 2019). Global sea surface (Trotter et al., 2016; Rasmussen et al., 2019) and mean surface temperatures (Judd et al., 2024).

In contrast, during the Aeronian, the decline in authigenic quartz content was accompanied by an increase in clay mineral abundance and a rise in temperature (Fig. 12). This is consistent with the low quartz content and high clay mineral content observed under the anomalously high temperatures of the Early Triassic (Isson et al., 2022). This suggests that the role of siliceous organisms in silicon burial weakened, potentially diminishing the suppression of reverse weathering, thereby leading to an increase in clay mineral content and global warming. In addition to organic carbon burial, volcanic activity, silicate weathering, and other factors, this study highlights the potential influence of siliceous ecosystems in the cooling process, implying that the driving mechanisms behind climate event may be more complex than previously understood.

## 6. Conclusions

This study emphasizes the dynamic behavior of biogenic silica in the Early Silurian, encompassing processes of dissolution and reprecipitation: opal dissolution coupled with microbubbles leads to the formation of discrete microcrystalline quartz grains, which then aggregate into clusters and evolve into larger aggregates. These results shed light on reconstructing early marine silicon cycles, where biogenic silica signifies siliceous organisms' activity, and its transformation into microcrystalline quartz serves as a potential silicon sink. Petrological and geochemical data suggest a rise in biogenic silica in the Upper Hirnantian–Rhuddanian, aligning with the proliferation of microcrystalline quartz and its aggregates, which may reflect the recovery of siliceous ecosystems during this interval. As siliceous ecosystems recovered, the amount of dissolved silicon participating in reverse weathering declined

markedly, thereby reducing CO<sub>2</sub> pressure at the ocean-atmosphere system. These observations could have critical implications for global climate dynamics, as enhanced silica burial may have prolonged cold climates.

## CRediT authorship contribution statement

**Huan Xu:** Writing – original draft, Methodology, Investigation, Data curation, Conceptualization. **Bo Ran:** Writing – original draft, Methodology, Funding acquisition, Conceptualization. **Terry T. Ison:** Writing – review & editing, Conceptualization. **Xinyang Chen:** Writing – review & editing, Visualization. **Chao Luo:** Methodology, Data curation. **Yi Li:** Investigation, Data curation. **Yiqing Zhu:** Visualization, Methodology. **Tong Sun:** Investigation, Data curation. **Yuyue Han:** Methodology, Data curation.

## Declaration of competing interest

The authors declare that they have no known competing financial interests or personal relationships that could have appeared to influence the work reported in this paper.

## Acknowledgements

The work was supported by the National Natural Science Foundation of China (Grant No. 42072129).

## Appendix A. Supplementary data

Supplementary data to this article can be found online at <https://doi.org/10.1016/j.palaeo.2025.113206>.

## Data availability

The authors confirm that all data necessary for supporting the scientific findings of this paper have been provided.

## References

- Adachi, M., Yamamoto, K., Sugisaki, R., 1986. Hydrothermal chert and associated siliceous rocks from the northern Pacific their geological significance as indication of ocean ridge activity. *Sediment. Geol.* 47 (1–2), 125–148. [https://doi.org/10.1016/0037-0738\(86\)90075-8](https://doi.org/10.1016/0037-0738(86)90075-8).
- Aller, R.C., 2014. Sedimentary diagenesis, depositional environments, and benthic fluxes. In: Turekian, H.D.H.K. (Ed.), *Treatise on Geochemistry*, second ed. Elsevier, Oxford, pp. 293–334.
- Bennig, L.G., Phoenix, V.R., Yee, N., Tobin, M.J., 2004. Molecular characterization of cyanobacterial silicification using synchrotron infrared micro-spectroscopy. *Geochim. Cosmochim. Acta* 68 (4), 729–741. [https://doi.org/10.1016/S0016-7037\(03\)00489-7](https://doi.org/10.1016/S0016-7037(03)00489-7).
- Bjorkum, P.A., Nadeau, P.H., 1998. Temperature controlled porosity/permeability reduction, fluid migration, and petroleum exploration in sedimentary basins. *APPEA J.* 38 (1), 453–465. <https://doi.org/10.1071/AJ97022>.
- Bjørlykke, K., 1998. Clay mineral diagenesis in sedimentary basins—a key to the prediction of rock properties. Examples from the North Sea Basin. *Clay Miner.* 33 (1), 15–34. <https://doi.org/10.1180/00985598545390>.
- Bjørlykke, K., Egeland, P.K., 1993. Quartz cementation in sedimentary basins. *AAPG Bull.* 77 (9), 1538–1548. <https://doi.org/10.1306/BDFF8EE8-1718-11D7-864500102C1865D>.
- Bopp, L., Aumont, O., Cadule, P., Alvain, S., Gehlen, M., 2005. Response of diatoms distribution to global warming and potential implications: a global model study. *Geophys. Res. Lett.* 32 (19). <https://doi.org/10.1029/2005GL023653>.
- Brenchley, P.J., Marshall, J.D., Carden, G.A.F., Robertson, D.B.R., Long, D.G.F., Meidla, T., Hints, L., Anderson, T.F., 1994. Bathymetric and isotopic evidence for a short-lived Late Ordovician glaciation in a greenhouse period. *Geology* 22 (4), 295–298. [https://doi.org/10.1130/0091-7613\(1994\)022<295:BAIEFA>2.3.CO;2](https://doi.org/10.1130/0091-7613(1994)022<295:BAIEFA>2.3.CO;2).
- Burland, J.B., 1990. On the compressibility and shear strength of natural clays. *Géotechnique* 40, 329–378. <https://doi.org/10.1680/geot.1990.40.3.329>.
- Chen, X., Rong, J., Li, Y., Boucot, A., 2004. Facies patterns and geography of the Yangtze region, South China, through the Ordovician and Silurian transition. *Palaeogeogr. Palaeoclimatol. Palaeoecol.* 204, 353–372. [https://doi.org/10.1016/S0031-0182\(03\)00736-3](https://doi.org/10.1016/S0031-0182(03)00736-3).
- Chen, X., Zhang, Y., Fan, J., Tang, L., Sun, H., 2012. Onset of the Kwangshian Orogeny as evidenced by biofacies and lithofacies. *Sci. China Earth Sci.* 55 (10), 1592–1600. <https://doi.org/10.1007/s11430-012-4490-4>.
- Chen, C., Wang, J., Algeo, T.J., Wang, Z., Tu, S., Wang, G., Yang, J., 2017. Negative δ<sup>13</sup>C<sub>carb</sub> shifts in Upper Ordovician (Hirnantian) Guanyinqiao Bed of South China linked to diagenetic carbon fluxes. *Palaeogeogr. Palaeoclimatol. Palaeoecol.* 487, 430–446. <https://doi.org/10.1016/j.palaeo.2017.09.030>.
- Chen, X., Chen, Q., Zhen, Y., Wang, H., Zhang, L., Zhang, J., Wang, W., Xiao, Z., 2018. Circumjacent distribution pattern of the Lungmachian graptolitic black shale (early Silurian) on the Yichang Uplift and its peripheral region. *Sci. China Earth Sci.* 61 (9), 1195–1203. <https://doi.org/10.1007/s11430-017-9222-x>.
- Chen, C., Wang, J., Algeo, T.J., Chen, X., Wang, Z., Ma, X., Cen, Y., Zhao, J., 2020. New evidence for compaction-driven vertical fluid migration into the Upper Ordovician (Hirnantian) Guanyinqiao bed of South China. *Palaeogeogr. Palaeoclimatol. Palaeoecol.* 550, 109746. <https://doi.org/10.1016/j.palaeo.2020.109746>.
- Chen, K., Yang, R., Bao, H., Dong, T., Jia, A., Hu, Q., Guo, X., He, S., 2023. Depositional-diagenetic process and their implications for pore development of Wufeng-Longmaxi shales in the Jiangdong block, Fuling shale gas field, SW China. *Mar. Pet. Geol.* 151, 106177. <https://doi.org/10.1016/j.marpetgeo.2023.106177>.
- Chen, C., Wang, J., Chen, X., Algeo, T.J., Wang, Z., Yang, W., Song, Q., 2024. Productivity and redox influences on the late Ordovician ‘Katian Extinction’ and ‘early Silurian Recovery’. *Palaeogeogr. Palaeoclimatol. Palaeoecol.* 642, 112176. <https://doi.org/10.1016/j.palaeo.2024.112176>.
- Closet, I., Brzezinski, M.A., Cardinal, D., Dapoigny, A., Jones, J.L., Robinson, R.S., 2022. A silicon isotopic perspective on the contribution of diagenesis to the sedimentary silicon budget in the Southern Ocean. *Geochim. Cosmochim. Acta* 327, 298–313. <https://doi.org/10.1016/j.gca.2022.04.010>.
- Conley, D.J., Frings, P.J., Fontorbe, G., Clymans, W., Stadmark, J., Hendry, K.R., Marron, A.O., De La Rocha, C.L., 2017. Biosilicification drives a decline of dissolved Si in the oceans through geologic time. *Front. Mar. Sci.* 4, 397. <https://doi.org/10.3389/fmars.2017.00397>.
- Day-Stirrat, R.J., Milliken, K.L., Dutton, S.P., Loucks, R.G., Hillier, S., Aplin, A.C., Schleicher, A.M., 2010. Open-system chemical behavior in deep Wilcox Group mudstones, Texas Gulf Coast, USA. *Mar. Pet. Geol.* 27 (9), 1804–1818. <https://doi.org/10.1016/j.earscirev.2018.12.002>.
- Delle Piane, C., Ansari, H., Li, Z., Mata, J., Rickard, W., Pini, R., Dewhurst, D.N., Sherwood, N., 2022. Influence of organic matter type on porosity development in the Wufeng-Longmaxi Shale: a combined microscopy, neutron scattering and physisorption approach. *Int. J. Coal Geol.* 249, 103880. <https://doi.org/10.1016/j.coal.2021.103880>.
- Deng, Y., Fan, J., Zhang, S., Fang, X., Chen, Z., Shi, Y., Wang, H., Wang, X., Yang, J., Hou, X., Wang, Y., Zhang, Y., Chen, Q., Yang, A., Fan, R., Dong, S., Xu, H., Shen, S., 2021. Timing and patterns of the great Ordovician biodiversification event and late Ordovician mass extinction: perspectives from South China. *Earth Sci. Rev.* 220, 103743. <https://doi.org/10.1016/j.earscirev.2021.103743>.
- Dong, T., He, S., Chen, M., Hou, Y., Guo, X., Wei, C., Han, Y., Yang, R., 2019. Quartz types and origins in the paleozoic Wufeng-Longmaxi Formations, Eastern Sichuan Basin, China: implications for porosity preservation in shale reservoirs. *Mar. Pet. Geol.* 106, 62–73. <https://doi.org/10.1016/j.marpetgeo.2019.05.002>.
- Dowey, P.J., Taylor, K.G., 2017. Extensive authigenic quartz overgrowths in the gas-bearing Haynesville-Bossier Shale, USA. *Sediment. Geol.* 356, 15–25. <https://doi.org/10.1016/j.sedgeo.2017.05.001>.
- Dowey, P.J., Taylor, K.G., 2020. Diagenetic mineral development within the upper Jurassic Haynesville-Bossier shale, USA. *Sedimentology* 67, 47–77. <https://doi.org/10.1016/j.sedgeo.2017.05.001>.
- Dunlea, A.G., Murray, R.W., Sauvage, J., Spivack, A.J., Harris, R.N., D'Hondt, S., 2015. Dust, volcanic ash, and the evolution of the South Pacific Gyre through the Cenozoic. *Paleceanography* 30 (8), 1078–1099. <https://doi.org/10.1002/2015PA002829>.
- Dunlea, A.G., Murray, R.W., Santiago Ramos, D.P., Higgins, J.A., 2017. Cenozoic global cooling and increased seawater Mg/ca via reduced reverse weathering. *Nat. Commun.* 8 (1), 844. <https://doi.org/10.1038/s41467-017-00853-5>.
- Emmings, J.F., Dowey, P.J., Taylor, K.G., Davies, S.J., Vane, C.H., Moss-Hayes, V., Rushton, J.C., 2020. Origin and implications of early diagenetic quartz in the Mississ., UK. *Mar. Pet. Geol.* 120, 104567. <https://doi.org/10.1016/j.marpetgeo.2020.104567>.
- Ergene, S.M., 2014. Lithologic Heterogeneity of the Eagle Ford Formation, South Texas. Master thesis, The University of Texas at Austin, 182 pp. <http://hdl.handle.net/2152/25752>.
- Finnegan, S., Bergmann, K., Eiler, J.M., Jones, D.S., Pike, D.A., Eisenman, I., Hughes, N., C., Tripathi, A.K., Fischer, W.W., 2011. The magnitude and duration of late Ordovician–early Silurian glaciation. *Science* 331 (6019), 903–906. <https://doi.org/10.1126/science.1200803>.
- Folk, R., 1974. Petrology of Sedimentary Rocks. Hemphill Pub. Co., Austin, Texas, p. 63.
- Frakes, L.A., Francis, J.E., Syktus, J.I., 1996. Climate Modes of the Phanerozoic. Cambridge Univ. Press, Cambridge.
- Gambacorta, G., Tricinatti, E., Torricelli, S., 2016. Anoxia controlled by relative sea-level changes: An example from the Mississippian Barnett Shale Formation. *Palaeogeogr. Palaeoclimatol. Palaeoecol.* 459, 306–320. <https://doi.org/10.1016/j.palaeo.2016.07.015>.
- Han, M., 2018. Study on Reservoirs Characteristics and Controlling Factors of WuFeng-Longmaxi Black Shale in Southern Sichuan Basin [PhD Dissertation]. Shandong University of Science and Technology, Qingdao, China (in Chinese).
- Han, Y., Ran, B., Liu, S., Li, Z., Ye, Y., Sun, W., Yang, D., Wang, S., 2021. Main controlling factors of organic-matter enrichment in the Ordovician-Silurian marine organic-rich mudrock in the Yangtze Block, South China. *Mar. Pet. Geol.* 127, 104959. <https://doi.org/10.1016/j.marpetgeo.2021.104959>.

- Handley, K.M., Turner, S.J., Campbell, K.A., Mountain, B.W., 2008. Silicifying biofilm exopolymers on a hot-spring microstromatolite: templating nanometer-thick laminae. *Astrobiology* 8 (4), 747–770. <https://doi.org/10.1089/ast.2007.0172>.
- Herrmann, A.D., Patzkowsky, M.E., Pollard, D., 2003. Obliquity forcing with 8–12 times preindustrial levels of atmospheric pCO<sub>2</sub> during the Late Ordovician glaciation. *Geology* 31 (6), 485–488. [https://doi.org/10.1130/0091-7613\(2003\)031<0485:OFWTPL>2.0.CO;2](https://doi.org/10.1130/0091-7613(2003)031<0485:OFWTPL>2.0.CO;2).
- Huang, Z., Li, Z., Shi, W., Yang, X., Wang, X., Young, S., 2023. Differential sedimentary mechanisms of upper Ordovician-lower Silurian shale in southern Sichuan Basin, China. *Mar. Pet. Geol.* 148, 106040. <https://doi.org/10.1016/j.marpetgeo.2022.106040>.
- Ikeda, M., Tada, R., Ozaki, K., 2017. Astronomical pacing of the global silica cycle recorded in Mesozoic bedded cherts. *Nat. Commun.* 8, 15532. <https://doi.org/10.1038/ncomms15532>.
- Isson, T.T., Planavsky, N.J., 2018. Reverse weathering as a long-term stabilizer of marine pH and planetary climate. *Nature* 560 (7719), 471–475. <https://doi.org/10.1038/s41586-018-0408-4>.
- Isson, T., Rauzi, S., 2024. Oxygen isotope ensemble reveals Earth's seawater, temperature, and carbon cycle history. *Science* 383 (6683), 666–670. <https://doi.org/10.1126/science.adg1366>.
- Isson, T.T., Planavsky, N.J., Coogan, L.A., Stewart, E.M., Ague, J.J., Bolton, E.W., Zhang, S., Mckenzie, N.R., Kump, L.R., 2020. Evolution of the global carbon cycle and climate regulation on earth. *Glob. Biogeochem. Cycles* 34 (2). <https://doi.org/10.1029/2019GB006061> e2018GB006061.
- Isson, T.T., Zhang, S., Lau, K.V., Rauzi, S., Tosca, N.J., Penman, D.E., Planavsky, N.J., 2022. Marine siliceous ecosystem decline led to sustained anomalous Early Triassic warmth. *Nat. Commun.* 13 (1), 3509. <https://doi.org/10.1038/s41467-022-31128-3>.
- Jin, Z., Yuan, Y., Sun, D., Liu, Q., Li, S., 2014. Models for dynamic evaluation of mudstone/shale cap rocks and their applications in the Lower Paleozoic sequences, Sichuan Basin, SW China. *Mar. Pet. Geol.* 49, 121–128. <https://doi.org/10.1016/j.marpetgeo.2013.10.001>.
- Judd, E.J., Tierney, J.E., Lunt, D.J., Montañez, I.P., Huber, B.T., Wing, S.L., Valdes, P.J., 2024. A 485-million-year history of Earth's surface temperature. *Science* 385 (6715), eadk3705. <https://doi.org/10.1126/science.adk3705>.
- Jurkowska, A., Świerczewska-Gładysz, E., 2020. New model of Si balance in the late cretaceous epicontinental European Basin. *Glob. Planet. Chang.* 186, 103108. <https://doi.org/10.1016/j.gloplacha.2019.103108>.
- Jurkowska, A., Świerczewska-Gładysz, E., 2024. The evolution of the marine Si cycle in the Archean-Palaeozoic—an overlooked Si source? *Earth Sci. Rev.* 248, 104629. <https://doi.org/10.1016/j.earscirev.2023.104629>.
- Kazmierczak, J., Kremer, B., Rakci, G., 2012. Late Devonian marine anoxia challenged by benthic cyanobacterial mats. *Geobiology* 10 (5), 371–383. <https://doi.org/10.1111/j.1472-4669.2012.00339.x>.
- Khan, M.Z., Feng, Q., Zhang, K., Guo, W., 2019. Biogenic silica and organic carbon fluxes provide evidence of enhanced marine productivity in the Upper Ordovician-Lower Silurian of South China. *Palaeogeogr. Palaeoclimatol. Palaeoecol.* 534, 109278. <https://doi.org/10.1016/j.palaeo.2019.109278>.
- Kidder, D.L., Erwin, D.H., 2001. Secular distribution of biogenic silica through the Phanerozoic: comparison of silica-replaced fossils and bedded cherts at the series level. *J. Geol.* 109 (4), 509–522. <https://doi.org/10.1086/320794>.
- Krug, A.Z., Patzkowsky, M.E., 2004. Rapid recovery from the Late Ordovician mass extinction. *Proc. Natl. Acad. Sci.* 101 (51), 17605–17610. <https://doi.org/10.1073/pnas.0405199102>.
- Kump, L.R., Brantley, S.L., Arthur, M.A., 2000. Chemical weathering, atmospheric CO<sub>2</sub>, and climate. *Annu. Rev. Earth Planet. Sci.* 28 (1), 611–667. <https://doi.org/10.1146/annurev.earth.28.1.611>.
- Lander, R.H., Larese, R.E., Bonnell, L.M., 2008. Toward more accurate quartz cement models: the importance of euhedral versus non-euhedral growth rates. *AAPG Bull.* 92, 1537–1563. <https://doi.org/10.1306/07160808037>.
- Liang, F., Zhao, Q., Zhang, Q., Wang, Y., Zhou, S., Qiu, Z., Liu, W., Ran, B., Sun, T., 2025. Controls of paleogeomorphology on organic matter accumulation as recorded in Ordovician-Silurian marine black shales in the western South China Block. *Mar. Pet. Geol.* 172, 107206. <https://doi.org/10.1016/j.marpetgeo.2024.107206>.
- Liu, W., Wu, J., Jiang, H., Zhou, Z., Luo, C., Wu, W., Li, X., Liu, S., Deng, B., 2021. Cenozoic exhumation and shale-gas enrichment of the Wufeng-Longmaxi formation in the southern Sichuan basin, western China. *Mar. Pet. Geol.* 125, 104865. <https://doi.org/10.1016/j.marpetgeo.2020.104865>.
- Longman, J., Mills, B.J., Manners, H.R., Gernon, T.M., Palmer, M.R., 2021. Late Ordovician climate change and extinctions driven by elevated volcanic nutrient supply. *Nat. Geosci.* 14 (12), 924–929. <https://doi.org/10.1038/s41561-021-00855-5>.
- Lv, D., Wang, L., Isbell, J.L., Lu, C., Li, P., Wang, Y., Zhang, Z., 2022. Records of chemical weathering and volcanism linked to paleoclimate transition during the Late Paleozoic Icehouse. *Glob. Planet. Chang.* 217, 103934. <https://doi.org/10.1016/j.gloplacha.2022.103934>.
- Lv, D., Zhao, Y., Steel, R.J., Jia, H., Raji, M., Zhang, Z., Ju, L., Gong, L., Wang, X., 2025. Massive organic carbon burial in the North China Basin is a main contributor to peak Late Paleozoic Ice Age in early Asselian. *Earth Planet. Sci. Lett.* 661, 119370. <https://doi.org/10.1016/j.epsl.2025.119370>.
- Ma, J., Shi, X., Lechte, M., Zhou, X., Wang, Z., Huang, K., Rudmin, M., Tang, D., 2022. Mesoproterozoic seafloor authigenic glauconite-berthierine: Indicator of enhanced reverse weathering on early Earth. *Am. Mineral.* 107 (1), 116–130. <https://doi.org/10.2138/am-2021-7904>.
- Metcalfe, I., 2006. Palaeozoic and Mesozoic tectonic evolution and palaeogeography of East Asian crustal fragments: the Korean Peninsula in context. *Gondwana Res.* 9, 24–46. <https://doi.org/10.1016/j.gr.2005.04.002>.
- Metwally, Y.M., Cheskakov, E.M., 2012. Clay mineral transformation as a major source for authigenic quartz in thermo-mature gas shale. *Appl. Clay Sci.* 55, 138–150.
- Meunier, A., Velde, B.D., 2013. Illite: Origins, Evolution and Metamorphism. Springer Science & Business Media.
- Milliken, K.L., Day-Stirrat, R.J., 2013. Cementation in mudrocks: Brief review with examples from cratonic basin mudrocks. <https://doi.org/10.1306/13401729H55252>.
- Milliken, K.L., Olson, T., 2017. Silica diagenesis, porosity evolution, and mechanical behavior in siliceous mudstones, Mowry Shale (Cretaceous), Rocky Mountains, USA. *J. Sediment. Res.* 87, 366–387. <https://doi.org/10.2110/jsr.2017.24>.
- Milliken, K.L., Esch, W.L., Reed, R.M., Zhang, T., 2012. Grain assemblages and strong diagenetic overprinting in siliceous mudrocks, Barnett Shale (Mississippian), Fort Worth Basin, Texas. *AAPG Bull.* 96 (8), 1553–1578. <https://doi.org/10.1306/120111111129>.
- Milliken, K.L., Ergene, S.M., Ozkan, A., 2016. Quartz types, authigenic and detrital, in the Upper cretaceous Eagle Ford Formation, South Texas, USA. *Sediment. Geol.* 339, 273–288. <https://doi.org/10.1016/j.sedgeo.2016.03.012>.
- Milliken, K.L., Reed, R.M., McCarty, D.K., Bishop, J., Lipinski, C., Fischer, T.B., Crousse, L., Reijenstein, H., 2019. Grain assemblages and diagenesis in the Vaca Muerta formation (Jurassic-Cretaceous), Neuquén basin, Argentina. *Sediment. Geol.* 380, 45–64. <https://doi.org/10.1016/j.sedgeo.2018.11.007>.
- Nie, H., Liu, Q., Li, P., Li, P., Ding, J., Sun, C., Zhai, C., Zhao, J., Dang, W., 2025. Quartz types, formation mechanism, and its effect on shale oil and gas enrichment: a review. *Earth Sci. Rev.* 261, 105011. <https://doi.org/10.1016/j.earscirev.2024.105011>.
- Peltonen, C., Marcussen, Ø., Bjørlykke, K., Jahren, J., 2009. Clay mineral diagenesis and quartz cementation in mudstones: the effects of smectite to illite reaction on rock properties. *Mar. Pet. Geol.* 26, 887–898. <https://doi.org/10.1016/j.marpetgeo.2008.01.021>.
- Peng, J., Hu, Z., Feng, D., 2024. Influence of quartz types on rock fabrics and bulk physical properties in organic-rich mudstone: a review. *Earth-Sci. Rev.*, 104670. <https://doi.org/10.1016/j.earscirev.2023.104670>.
- Pichevin, L.E., Ganeshram, R.S., Geibert, W., Thunell, R., Hinton, R., 2014. Silica burial enhanced by iron limitation in oceanic upwelling margins. *Nat. Geosci.* 7 (7), 541–546. <https://doi.org/10.1038/geo2181>.
- Popov, L.E., Cocks, L.R.M., 2017. Late Ordovician palaeogeography and the positions of the Kazakh terranes through analysis of their brachiopod faunas. *Acta Geol. Pol.* 67, 323–380. <https://doi.org/10.1515/agp-2017-0020>.
- Qiu, Z., Liu, B., Dong, D., Lu, B., Yawar, Z., Chen, Z., Schieber, J., 2020. Silica diagenesis in the Lower Paleozoic Wufeng and Longmaxi Formations in the Sichuan Basin, South China: Implications for reservoir properties and paleoproductivity. *Mar. Pet. Geol.* 121, 104594. <https://doi.org/10.1016/j.marpetgeo.2020.104594>.
- Rafiee, M., Löhr, S., Baldermann, A., Webster, R., Kong, C., 2020. Quantitative petrographic differentiation of detrital vs diagenetic clay minerals in marine sedimentary sequences: implications for the rise of biotic soils. *Precambrian Res.* 350, 105948. <https://doi.org/10.1016/j.precamres.2020.105948>.
- Ran, B., Liu, S., Jansa, L., Sun, W., Yang, D., Ye, Y., Wang, S., Luo, C., Zhang, X., Zhang, C., 2015. Origin of the Upper Ordovician-lower Silurian cherts of the Yangtze block, South China, and their palaeogeographic significance. *J. Asian Earth Sci.* 108, 1–17. <https://doi.org/10.1016/j.jseas.2015.04.007>.
- Rasmussen, C.M., Kröger, B., Nielsen, M.L., Colmenar, J., 2019. Cascading trend of early Paleozoic marine radiations paused by late Ordovician extinctions. *Proc. Natl. Acad. Sci. USA* 116 (15), 7207–7213. <https://doi.org/10.1073/pnas.1821123116>.
- Rudnick, R.L., Gao, S., 2014. Composition of the continental crust. In: *Treatise on Geochemistry, second edition* 4, pp. 1–51.
- Schieber, J., Krinsley, D., Riciputi, L., 2000. Diagenetic origin of quartz silt in mudstones and implications for silica cycling. *Nature* 406, 981–985. <https://doi.org/10.1038/35023143>.
- Sheehan, P.M., 2001. The late Ordovician mass extinction. *Annu. Rev. Earth Planet. Sci.* 29, 331–364. <https://doi.org/10.1146/annurev.earth.29.1.331>.
- Tang, T., Kisslinger, K., Lee, C., 2014. Silicate deposition during decomposition of cyanobacteria may promote export of picophytoplankton to the deep ocean. *Nat. Commun.* 5 (1), 4143. <https://doi.org/10.1038/ncomms5143>.
- Taylor, S.R., McLennan, S.M., 1985. *The Continental Crust: Its Composition and Evolution*. Blackwell, Oxford, p. 312.
- Thyberg, B., Jahren, J., Winje, T., Bjørlykke, K., Faleide, J.I., Marcussen, Ø., 2010. Quartz cementation in Late Cretaceous mudstones, northern North Sea: changes in rock properties due to dissolution of smectite and precipitation of micro-quartz crystals. *Mar. Pet. Geol.* 27, 1752–1764. <https://doi.org/10.1016/j.marpetgeo.2009.07.005>.
- Tréguer, P.J., De La Rocha, C.L., 2013. The world ocean silica cycle. *Annu. Rev. Mar. Sci.* 5 (1), 477–501. <https://doi.org/10.1146/annurev-marine-121211-172346>.
- Tréguer, P., Bowler, C., Moriceau, B., Dutkiewicz, S., Gehlen, M., Aumont, O., Jahn, O., 2017. Influence of diatom diversity on the ocean biological carbon pump. *Nat. Geosci.* 11, 27. <https://doi.org/10.1038/s41561-017-0028-x>.
- Tréguer, P.J., Sutton, J.N., Brzezinski, M., Charette, M.A., Devries, T., Dutkiewicz, S., Ehler, C., Hawkings, J., Leynaert, A., Liu, S.M., 2021. Reviews and syntheses: the biogeochemical cycle of silicon in the modern ocean. *Biogeosciences* 18, 1269–1289. <https://doi.org/10.5194/bg-18-1269-2021>.
- Trotter, J.A., Williams, I.S., Barnes, C.R., Maennik, P., Simpson, A., 2016. New conodont δ<sup>18</sup>O records of Silurian climate change: implications for environmental and biological events. *Palaeogeogr. Palaeoclimatol. Palaeoecol.* 443, 34–48. <https://doi.org/10.1016/j.palaeo.2015.11.011>.

- Trower, E.J., Strauss, J.V., Sperling, E.A., Fischer, W.W., 2021. Isotopic analyses of Ordovician–Silurian siliceous skeletons indicate silica-depleted Paleozoic oceans. *Geobiology* 19 (5), 460–472. <https://doi.org/10.1111/gbi.12449>.
- Van den Boorn, S.H., van Bergen, M.J., Nijman, W., Vroon, P.Z., 2007. Dual role of seawater and hydrothermal fluids in early Archean chert formation: evidence from silicon isotopes. *Geology* 35 (10), 939–942. <https://doi.org/10.1130/G24096A.1>.
- Velde, B., 1996. Compaction trends of clay-rich deep sea sediments. *Mar. Geol.* 133, 193–201. [https://doi.org/10.1016/0025-3227\(96\)00020-5](https://doi.org/10.1016/0025-3227(96)00020-5).
- Weaver, C.E., 1967. Potassium, illite and the ocean. *Geochim. Cosmochim. Acta* 31 (11), 2181–2196. [https://doi.org/10.1016/0016-7037\(67\)90060-9](https://doi.org/10.1016/0016-7037(67)90060-9).
- Wedepohl, K.H., 1971. Environmental influences on the chemical composition of shales and clays. *Phys. Chem. Earth* 333.
- Wei, G.Y., Wei, W., Wang, D., Li, T., Yang, X., Shields, G.A., Zhang, F., Li, G., Chen, T., Yang, T., Ling, H.F., 2020. Enhanced chemical weathering triggered an expansion of euxinic seawater in the aftermath of the Sturtian glaciation. *Earth Planet. Sci. Lett.* 539, 116244. <https://doi.org/10.1016/j.epsl.2020.116244>.
- Williams, L.A., Crerar, D.A., 1985. Silica diagenesis; II, general mechanisms. *J. Sediment. Res.* 55, 312–321. <https://doi.org/10.1306/212F86B1-2B24-11D7-8648000102C1865D>.
- Williams, L.A., Parks, G.A., Crerar, D.A., 1985. Silica diagenesis; I, solubility controls. *J. Sediment. Res.* 55, 301–311. <https://doi.org/10.1306/212F86AC-2B24-11D7-8648000102C1865D>.
- Worden, R., Morad, S., 2000. Quartz Cementation in Oil Field Sandstones: a Review of the Key Controversies. Wiley Online Library. <https://doi.org/10.1002/9781444304237.ch1>.
- Worden, R.H., French, M.W., Mariani, E., 2012. Amorphous silica nanofilms result in growth of misoriented microcrystalline quartz cement maintaining porosity in deeply buried sandstones. *Geology* 40, 179–182. <https://doi.org/10.1130/G32661.1>.
- Wright, A.M., Spain, D., Ratcliffe, T., 2010. Application of inorganic whole rock geochemistry to shale resource plays. In: Canada Unconventional Resources & International Petroleum Conference, Calgary, Alberta, October 19–21, 2010, SPE Paper 137946. <https://doi.org/10.2118/137946-MS> (18 pp.).
- Xu, H., Zhou, W., Hu, Q., Yi, T., Ke, J., Zhao, A., Lei, Z., Yu, Y., 2021. Quartz types, silica sources and their implications for porosity evolution and rock mechanics in the Paleozoic Longmaxi Formation shale, Sichuan Basin. *Mar. Pet. Geol.* 128, 105036. <https://doi.org/10.1016/j.marpetgeo.2021.105036>.
- Yan, D., Chen, D., Wang, Q., Wang, J., 2009. Geochemical changes across the Ordovician–Silurian transition on the Yangtze platform, South China. *Sci. China Ser. D* 52 (1), 38–54. <https://doi.org/10.1007/s11430-008-0143-z>.
- Yan, D., Chen, D., Wang, Q., Wang, J., 2010. Large-scale climatic fluctuations in the latest Ordovician on the Yangtze block, South China. *Geology* 38 (7), 599–602. <https://doi.org/10.1130/G30961.1>.
- Yan, D., Wang, H., Fu, Q., Chen, Z., He, J., Gao, Z., 2015. Organic matter accumulation of Late Ordovician sediments in North Guizhou Province, China: sulfur isotope and trace element evidences. *Mar. Pet. Geol.* 59, 348–358. <https://doi.org/10.1016/j.marpetgeo.2014.09.017>.
- Yang, S., Hu, W., Fan, J., Deng, Y., 2022. New geochemical identification fingerprints of volcanism during the Ordovician–Silurian transition and its implications for biological and environmental evolution. *Earth Sci. Rev.* 228, 104016. <https://doi.org/10.1016/j.earscirev.2022.104016>.
- Yao, W.H., Li, Z.X., Li, W.X., Su, L., Yang, J.H., 2015. Detrital provenance evolution of the Ediacaran–Silurian Nanhua foreland basin, South China. *Gondwana Res.* 28 (4), 1449–1465. <https://doi.org/10.1016/j.gr.2014.10.018>.
- Yin, Y.S., Wei, G.Y., von Strandmann, P.A.P., Lechte, M.A., Hohl, S.V., Lin, Y.B., Li, D., Chen, T.Y., Yang, T., Zhang, F.F., Isson, T.T., Zhang, H., Cai, Y.F., Ling, H.F., 2023. Widespread clay authigenesis and highly congruent silicate weathering in the Marinoan aftermath. *Earth Planet. Sci. Lett.* 623, 118423. <https://doi.org/10.1016/j.epsl.2023.118423>.
- Zan, B., Mou, C., Lash, G.G., Wang, Q., Wang, X., Le Heron, D.P., Yan, J., Zhang, Z., Hou, Q., Xia, Y., Yao, S., 2024. Upwelling-driven biogenic silica accumulation in the Yangtze Sea, South China during late Ordovician to early Silurian time: a possible link with the global climatic transitions. *Sediment. Geol.* 461, 106571. <https://doi.org/10.1016/j.sedgeo.2023.106571>. Get rights and content.
- Zhang, B., Yao, S., Wignall, P.B., Hu, W., Ding, H., Liu, B., Ren, Y., 2018. Widespread coastal upwelling along the Eastern Paleo-Tethys Margin (South China) during the Middle Permian (Guadalupian): implications for organic matter accumulation. *Mar. Pet. Geol.* 97, 113–126. <https://doi.org/10.1016/j.marpetgeo.2018.06.025>.
- Zhang, J., Li, C., Zhong, Y., Wu, X., Fang, X., Liu, M., Chen, D., Gill, B.C., Algeo, T.J., Lyons, T.W., Zhang, Y., Tian, H., 2024. Linking carbon cycle perturbations to the Late Ordovician glaciation and mass extinction: a modeling approach. *Earth Planet. Sci. Lett.* 631, 118635. <https://doi.org/10.1016/j.epsl.2024.118635>.
- Zou, C., Zhu, R., Chen, Z.Q., Ogg, J.G., Wu, S., Dong, D., Qiu, Z., Wang, Y., Wang, L., Lin, S., Cui, J., Su, L., Yang, Z., 2019. Organic-matter-rich shales of China. *Earth Sci. Rev.* 189, 51–78. <https://doi.org/10.1016/j.earscirev.2018.12.002>.